Journal of Hydrology: Regional Studies 44 (2022) 101247

Contents lists available at ScienceDirect

Journal of Hydrology: Regional Studies

journal homepage: www.elsevier.com/locate/ejrh

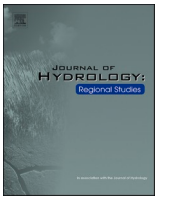

Estimation of flood-exposed population in data-scarce regions combining satellite imagery and high resolution hydrological-hydraulic modelling: A case study in the Licungo basin (Mozambique)

Luis Cea *, Manuel Álvarez, Jerónimo Puertas

Water and Environmental Engineering Group, Department of Civil Engineering, Universidade da Coruña, Spain

ARTICLE INFO

Keywords:
Tropical storms
Flood hazard
Global Digital Elevation Models
Sentinel-1 imagery
Iber model
Data-scarce regions

ABSTRACT

Study Region: Licungo basin (Mozambique)
Study Focus: The Licungo basin (23,263 km^2) suffers frequent severe flooding due to tropical storms, in a country that is among the world's most vulnerable in terms of exposure to weather-related hazards and climate change. We propose a methodology for the estimation of the population exposed to flooding at the catchment scale in data-scarce regions, combining satellite imagery with integrated high-resolution hydrological-hydraulic modelling. All the input data needed are retrieved from freely-available global satellite products. The numerical model is also freeware. The methodology is therefore replicable worldwide. An estimate of the flood extent and exposed population during Tropical Storm Ana (January 2022) is presented as a case study.
New Hydrological Insights for the Region: Current freely-available satellite products in combination with high-resolution hydrological-hydraulic models can be used to estimate the population exposed to flooding in the whole catchment. This estimate is more realistic than the one obtained using satellite imagery alone, since satellite images are very rarely taken at the time of maximum flooding. Using the proposed methodology, we estimate that over 273,000 people (out of 1.5 million) were exposed to flooding in the Licungo basin during Tropical Storm Ana. This represents 18% of the basin population and is 8 times larger than the estimate obtained using only the available satellite images.

1. Introduction

Vulnerability to river floods has increased throughout whole world in recent decades, but most intensively in developing countries (Cao et al., 2022; Douglas et al., 2008; Di Baldassarre et al., 2010; Rentschler et al., 2022; Tate et al., 2021; Tramblay et al., 2014; Wing et al., 2018). Moreover, a number of studies indicate that flood risk is expected to increase further in coming decades due to climate change, urbanization of river floodplains and changes in land use at the catchment scale (Areu-Rangel et al., 2019; Arnell and Gosling, 2016; Hirabayashi et al., 2013; Jenkins et al., 2017; Jongman et al., 2012; Liu et al., 2018). In this global context, African countries are especially exposed to flood damage due to the social and economic vulnerability of their communities and to the extreme magnitude of the flood events in large rivers and basins (Revilla-Romero et al., 2014). One example here is Mozambique, which occupies the 8th

* Correspondence to: E.T.S. Ingeniería de Caminos Canales y Puertos, Campus de Elviña, s/n, 15071 A Coruña, Spain.
E-mail address: luis.cea@udc.es (L. Cea).

https://doi.org/10.1016/j.ejrh.2022.101247
Received 14 July 2022; Received in revised form 17 October 2022; Accepted 20 October 2022
Available online 25 October 2022

position in a ranking of 178 countries in the Ecological Threat Report Index, a composite risk index based on 5 indicators (rapid population growth, water risk, food risk, temperature anomalies and natural disasters) that together measure the impact of ecological threats that countries will face between now and 2050 (Institute for Economics and Peace, 2021). According to the Ecological Threat Report, the population of Mozambique is expected to double over the next 30 years (from 32.2 million in 2021 to 65.3 million in 2050). A significant proportion of the population lives close to the river network, this in order to have access to surface water resources and to fertile lands, since subsistence farming constitutes the food base for many rural communities. As a consequence of all this, in 2020 the country had a prevalence of food insecurity of 71 % (10th highest in the world) and a prevalence of undernourishment of 31 % (13th highest in the world) (Institute for Economics and Peace, 2021).

For these reasons, in recent years several developing countries, including Mozambique, have made significant efforts to put Disaster Risk Reduction policies in place, including the evaluation of flood risk and the establishment of flood mitigation measures. This has been supported by funds from the European Commission and EU Member States, the U.S. Agency for International Development, the World Bank, and various NGOs. One example of this is the intervention in the Licungo basin (Mozambique) carried out by the Humanitarian Implementation Plan in 2018, which was supported by the Directorate-General for European Civil Protection and Humanitarian Operations (ECHO), the main objective being the strengthening of local preparedness and response capacities by linking early warning to early action. To this end, the identification of flood-prone areas, population exposed to flood risk, main infrastructures affected by floods, and safe evacuation routes all contribute significantly to the development and improvement of disaster management plans by the local and regional authorities. Such information also contributes to the implementation of flood early warning systems (EWS), a type of flood mitigation measure that has been implemented in recent years in many developed and underdeveloped countries, both on the local level (Fraga et al., 2020; González-Cao et al., 2019; Cools et al., 2012; Krajewski et al., 2017) and at a national or transnational scale (Alfieri et al., 2013; Weerts et al., 2011; Wu et al., 2014; Thielen et al., 2009).

The evaluation of flood hazard in large basins is usually done by coupling a hydrological model that computes the water discharge along the river network of the whole catchment with a 2D hydrodynamic model that transforms water discharge into water depths, velocities and flood extent at the river reach scale (Bermúdez et al., 2017; Komi et al., 2017; Nogherotto et al., 2019). The use of lumped hydrological models in data-scarce regions is very constrained, due to the high dependency of such models on the availability of observed data for the calibration of parameters (Merz et al., 2011). On the other hand, physically-based distributed models are, to a certain degree, less dependent on the calibration of input parameters, and can therefore be useful tools to estimate flood hazard in regions where hydrometric data are scarce (Cornelissen et al., 2013). Nonetheless, they require large amounts of spatially distributed data to define the catchment topography, land uses and soil types. Regarding the evaluation of water depths and velocities at the river reach scale, the most commonly used models today are those based on the2D fully dynamic shallow water Eq. (2D-SWE) due to the capacity of these to reproduce complex local flow patterns, although alternatives are available, including different simplifications of the 2D-SWE, as well as 1D-2D coupled models. An alternative to the coupled hydrologic/hydrodynamic modelling approach is to perform an integrated hydrological/hydrodynamic simulation at the catchment scale. Until recently this was prohibitive because of the computational cost of modelling such a large domain with a hydrodynamic model, but advances in High Performance Computing (HPC) and the development of new numerical schemes for solving the 2D-SWE at the catchment scale including rainfall and infiltration processes, opens up the possibility of modelling rainfall-runoff transformation and river hydraulics within a single integrated simulation over an entire catchment (Cea and Blade, 2015; García-Feal et al., 2018; Khaing et al., 2019; Xia et al., 2019). A review of flood hazard modelling approaches can be found in Cea and Costabile (2022) and Teng et al. (2017).

However, one of the main handicaps in the improvement of flood management in developing countries, and particularly in Africa, is the scarcity of quality hydrological and meteorological data, which precludes a robust and accurate calibration of hydrological and hydraulic flood hazard models (Komi et al., 2017; Sampson et al., 2015; Sanyal et al., 2014; Tramblay et al., 2014). On the other hand, over the last decade a large number of satellite remote sensing data related to water resources has been made available by international institutions and agencies, such as the National Aeronautics and Space Administration (NASA,) the European Space Agency (ESA) and the Japan Aerospace Exploration Agency (JAXA). These data include digital terrain models (DTM), quantitative precipitation estimations (QPE), land uses, soil types, soil moisture and surface water extent, among others. The spatial and temporal resolution of these data products is not as detailed and accurate as data from national observation networks in developed countries, but they are of great value in conducting flood hazard studies in developing countries or at a transnational scale (Dottori et al., 2016; Kugler and De Groeve, 2007; Kundu et al., 2015; Pappenberger et al., 2010; Sakamoto et al., 2007; Sampson et al., 2015; Winsemius et al., 2013; Yamazaki et al., 2011).

In addition to the characterisation of flood hazard, flood risk management plans require information on vulnerability and population exposure to floods. To date, those variables have received far less attention than flood hazard (Smith et al., 2019), even though they provide information that is essential as a means of establishing emergency plans and of estimating economic and social losses. Detailed maps of the spatial distribution of population (Calka et al., 2017; Winsemius et al., 2013) and transport infrastructures are of great value in evaluating the real exposure of a population to floods and the safest routes of evacuation in case of flooding (Watik and Jaelani, 2019). For this purpose, several population data sets are currently available (Calka et al., 2017; Smith et al., 2019).

The main purpose of the present study is to propose a methodology for the estimation of the population exposed to river flooding at the catchment scale in data-scarce regions, combining satellite imagery with an integrated high-resolution hydrological-hydraulic modelling approach based on the model Iber (Bladé et al., 2014; García-Feal et al., 2018). All the input data needed to apply the proposed methodology is retrieved from remote sensing open data sources at the global scale. The estimate of the flood extent and population affected by the inundation caused by the recent Tropical Storm Ana (January 2022) in the Licungo basin (Mozambique, 23, 263 km^2) is presented as a case study. Over a 24-hour period this Tropical Storm left a basin-averaged rainfall depth of 200 mm, reaching values of 350 mm at certain locations. The Licungo basin suffers flooding almost every year as a consequence of tropical

storms and cyclones, this in a country with one of the highest exposures to weather-related hazards (flooding, cyclones and drought) and climate change in the world. According to the International Disaster Database (CRED, 2022), floods and storms represent, respectively, 35.6 % and 23.7 % of the 118 natural disasters that have affected Mozambique over the last 56 years (1967–2022). The death toll associated with these closely related events in that period exceeds 100,000 people, while the total population affected was over 40 million, with economic losses estimated as 5.6 billion USD, representing 56.2 % of the total losses due to natural hazards in Mozambique. Whereas the present study focusses on the Licungo basin, the methodology proposed can be applied worldwide, since all the data and software required are freely available on the world wide web, and is therefore of especial interest in data-scarce regions and developing countries.

The following sections of the paper are organized thus. Section 2 presents a description of the Licungo basin and the main facts relating to Tropical Storm Ana. The methodology, open data sources and numerical model used in this study, plus their relation to other available data packages and models, is described in Section 3. In Section 4 we present and discuss the results related to flood extent and population affected by Tropical Storm Ana. Finally, Section 5 summarizes the main conclusions, including the advantages and limitations of the study.

2. Case study

Mozambique is a country with a high exposure to natural hazards and climate variability (World Bank, 2019a,b), and is a paradigm of Southeast Africa vulnerability to floods. Over 60% of its population is concentrated on the coastline, which is located on the path of tropical cyclones (TC) and tropical storms (TS) that form in, or pass through, the western part of the Indian Ocean (WMO, 2019). The country's exposure and vulnerability to floods is exacerbated by its relatively flat topography and scarce vegetation cover.

On average, one TS or TC hits the coast of Mozambique every two years between the months of October and April. However, the frequency of these tropical events has increased in recent years due to higher ocean temperatures brought about by climate change. In the first months of 2022 Mozambique was affected by two TS and one TC: TS Ana (GDACS, 2022a; OCHA, 2022a), TS Dumako (OCHA, 2022b) and TC Gombe (GDACS, 2022b; OCHA, 2022c). These three events had an impact on extensive areas of Central and North Mozambique. The regions of Zambezia and Nampula were affected by all three of them within a period of approximately two months. As a consequence, and according to the estimates of the National Institute for Disaster Management of Mozambique (INGD), over one million people were affected, around 10,000 people were displaced, and more than 100 people died. The floods affected over 200,000 ha, with serious damages to crop production and food security. According to the latest data released by the INGD, these three storms also destroyed 153,611 houses, damaged 95 health centres, 46 water supply systems, 2902 power poles, 4436 km of roads and 781 schools (impacting a total of 353,485 students).

The Licungo basin is located in northern Mozambique and has an area of approximately 23,263 km^2 (Fig. 1). The axis of the basin

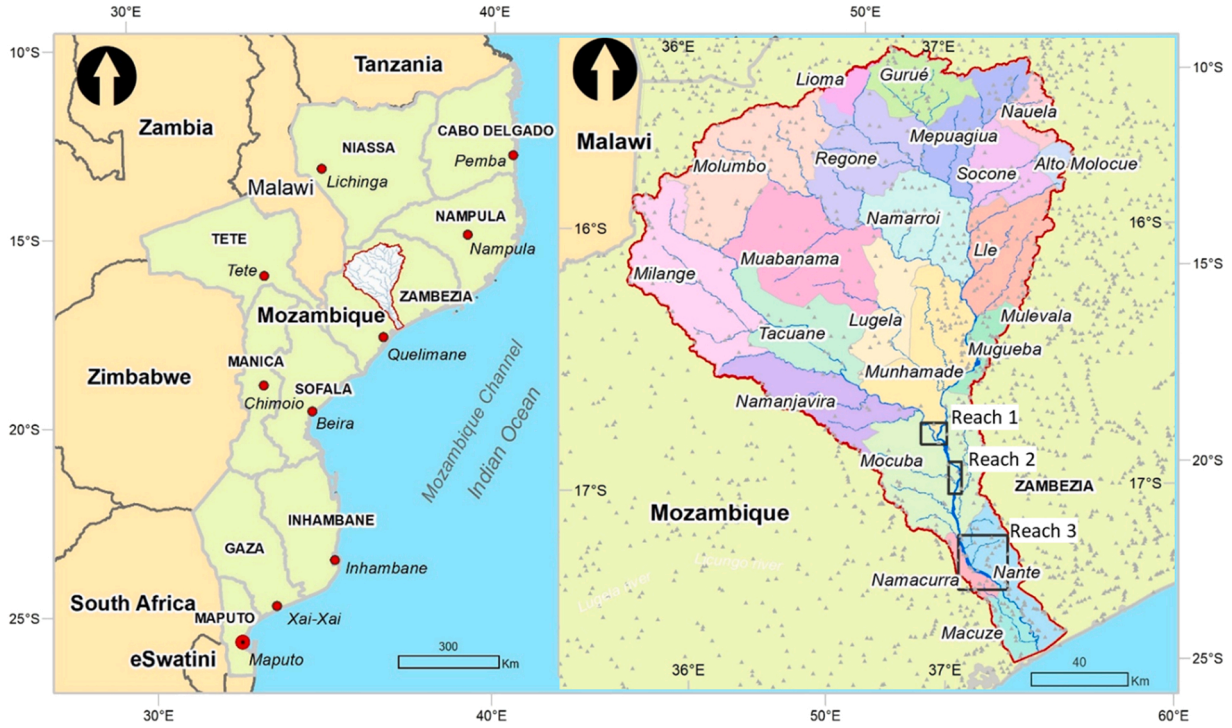

Fig. 1. Location map of the Licungo catchment within Mozambique (left). Administrative Posts within the Licungo basin and location of the three reaches (Reach 1, 2 and 3) used for the analysis of results at the reach scale (right).

follows an NW - SE orientation and is 343 km long. The average altitude is 474 m above mean sea level, with the highest altitude at 2348 m. The average slope of the basin hills is 10.6 %, which can be described as Moderately Sloping. Approximately 58% of the basin has a Flat to Undulating topography, with slopes ranging from 0 % to 8 %. The Mozambique National Water Resources Plan identifies the Licungo as one of the 11 basins in the country most exposed to flood damage. Over the last 52 years, the Licungo basin has experienced catastrophic floods in the following years: 1970, 1984, 1995, 1998, 2014, 2015, 2019 and 2022. Among these, the most severe in terms of material, economic and human life damages occurred in 2015, and was associated with the tropical cyclone events Chedza and Bansi (DRRT, 2015). Recently, during the first trimester of 2022 and barely one month apart, the aforementioned TS Ana, TS Dumako and TC Gombe caused severe flooding and extensive damage in the basin.

According to the Köppen Geiger climate classification, the Licungo is located in a Tropical Savanna area. The average annual precipitation over the basin in the period 1981–2010, as estimated using the CHIRPS (Climate Hazards Centre InfraRed Precipitation with Station data) pentadal data set (Funk et. al, 2015) was 1518 mm, although there are regions in the centre and northeast of the basin in which the annual precipitation exceeds 2000 mm. The rainy season extends from October to March, in which about 80 % of total annual precipitation is typically experienced.

The basin is divided into 9 administrative Districts, these subdivided into a total of 22 Administrative Posts (AP), as shown in Fig. 1. The main population settlements are the cities of Mocuba, located at the confluence of the Licungo and Lugela rivers in the central part of the basin, and Gurué , in the northeast of the basin. The communities most vulnerable to flooding are those located in the middle and lower part of the basin (AP of Mocuba, Mugeba, Munhamade, Macuze, Namacurra and Nante).

In this study we focused on the evaluation of the effects of TS Ana in terms of population exposed to flooding within the Licungo basin. TS Ana took place between 24/01/2022 and 27/01/2022, leaving a basin-averaged rainfall depth of 200 mm in the first 24 h, and maximum rainfall depths of 350 mm at certain locations in the basin. According to the report issued on 14/02/2022 by the United Nations Office for the Coordination of Humanitarian Affairs (OCHA), TS Ana affected 185,429 people, leading to 38 deaths and injuries to a further 207 people, and destroyed 11,757 houses across the whole of Mozambique (OCHA, 2022a). The final numbers were probably even greater, given that this evaluation of damages was carried out just two weeks after the storm.

3. Data and methodology

3.1. Open data sources

The different satellite data sets used in this study are listed in Table 1, which also includes the URL where each data set can be accessed freely. The spatial resolution varies from 10 m to 10 km, depending on the data set. The following sections describe the most pertinent features of each data set for hydrological modelling purposes, as well as the relations to alternative satellite data sources.

3.1.1. Digital elevation model

Having a Digital Elevation Model with the highest available spatial resolution and vertical accuracy is probably the most important requirement for a successful flood simulation. This is especially true for data-scarce regions, where the availability of topographic data are limited to satellite remote sensors (Álvarez et al., 2017). Currently, there are several Global Digital Elevation Models (GDEM) that were obtained after processing data from satellite missions carried out by international space agencies. Some of the GDEM commonly used in hydrological studies are those issued by the Shuttle Radar Topography Mission (SRTM) from the US Geological Survey (Farr et al., 2007), the Advanced Spaceborne Thermal Emission and Reflection Radiometer (ASTER) from NASA (Tadono et al., 2014), the Advanced Land Observing Satellite (ALOS) from JAXA (Abrams, 2000), and the TanDEM-X data set from the German Aerospace Agency and Airbus (Rizzoli et al., 2017).

The SRTM data were obtained during a single 11-day mission in 2000, and is the basis for several GDEM that have been processed by different algorithms (e.g. void and sink filling, removal of outliers, smoothing of elevation, or merging with other satellite data, among others) in order to reduce vertical errors and to facilitate the application of the data to hydrological studies. Some SRTM-based GDEM commonly used in hydrological studies are SRTM v3, the one provided by the CGIAR Consortium for Spatial Information (CGIAR-CSI), the Bare Earth DEM (O'Loughlin et al., 2016), the Multi-Error-Removed-Improved-Terrain (MERIT) (Yamazaki et al., 2017), and the recently released NASADEM, which was obtained after reprocessing the entire original SRTM raw data set with improved processing algorithms, and is expected to be NASA's finest resolution (1 arc-sec, roughly 30 m) freely-available GDEM product for the foreseeable future. The SRTM data are also used in the HydroSHEDS package (Hydrological data and maps based on SHuttle Elevation Derivatives at multiple Scales), that includes global digital data layers as catchment boundaries, river networks, and

Table 1
Data sets and sources used in the numerical model.

Variable	Data set	Resolution	Source
DEM	Copernicus GLO-30	30 m	https://panda.copernicus.eu/web/cds-catalogue
Rainfall	GPM IMERG Final Precipitation L3	10 km, 30 min	https://disc.gsfc.nasa.gov
Land Cover	GlobCover	20 m	http://due.esrin.esa.int/page_globcover.php
Infiltration	GCN250	250 m	https://doi.org/10.6084/m9.figshare.7756202.v1
Flood extent	Sentinel-1A	10 m	https://scihub.copernicus.eu/dhus/#/home
Population	WorldPop	90 m	https://hub.worldpop.org/geodata/summary?id= 6404

lakes at multiple resolutions and scales (Lehner et al., 2008). Most of these DEM products (CGIAR, Bare Earth, MERIT, HydroSHEDS v1) are provided at 3 arc-sec resolutions (roughly 90 m), while only two (NASADEM and SRTM v3) at 1 arc-sec (roughly 30 m).

The TanDEM-X mission is far more recent than SRTM (the data were obtained between 2011 and 2015) and consists of two twin satellites (TanDEM-X and TerraSAR-X) that orbit the earth in close formation (Krieger et al., 2013; Zink et al., 2021). The main practical improvements over SRTM is that the TanDEM-X mission covers the entire Earth (also the highest latitudes, above 60^{o} N and below 60^{o} S) with a higher vertical accuracy (lower than 2 m) and a horizontal resolution of 12 m (although data with this resolution is not freely available). The original version of the TanDEM-X DEM is a non-edited product, which leads to local errors that typically appear on ridges and canyons (Marešová et al., 2021). Airbus Defence and Space released an edited commercial version of TanDEM-X with a spatial resolution of 12 m, known as WorldDEM™, which significantly improves the vertical accuracy of other available GDEMs (Bayburt et al., 2017), and which was used by the European Space Agency (ESA) to generate three Copernicus DEMs: EEA-10 (0.4 arc-sec), GLO-30 (1 arc-sec), and GLO-90 (3 arc-sec), the first of these covering only European states. TanDEM-X data are also being used to produce the next version of the HydroSHEDS package.

Recent studies indicate that Copernicus GLO-30 is the DEM with the best overall performance that is freely available. Guth and Geoffroy (2021) assessed the performance of Copernicus GLO-30 in eight regions representing a variety of reliefs, and concluded that it provides the best representation of the terrain when compared to other commonly used 1 arc-sec DEMs (ALOS, ASTER, NASADEM, and SRTM v3). Maresova et al. (2021) compared the performance of several GDEMs in three European mountain ranges (Alps, Pyrenees and Carpathians), showing that Copernicus GLO-30 gives a more accurate representation of the terrain than TanDEM-X, SRTM v3, and NASADEM. Garrote (2022) analysed the suitability for hydraulic modelling of eight freely-available GDEMs in a river reach of the Licungo basin and, in line with the previous studies, concluded that Copernicus GLO-30 is clearly the best option for hydraulic modelling in this region. Although we didn't perform a detailed comparison of all the previous GDEMs for modelling purposes in the Licungo basin, we did compare the topography and water depths obtained with SRTM v3 and Copernicus GLO-30, concluding that GLO-30 clearly outperforms SRTM v3 in this case, with a far more precise and less noisy definition of the main channel and floodplains (Fig. 2).

Considering the previous studies, and especially the comparative DEM analysis presented by Garrote (2022) applied to flood modelling in a reach of the Licungo river, we used Copernicus GLO-30 to represent the topography of the whole Licungo catchment (Fig. 2) in the integrated hydrological-hydraulic modelling performed with Iber.

3.1.2. Rainfall

A correct characterization of the spatial and temporal variability of rainfall is of utmost importance for the estimation of flood hazard. The spatial and temporal resolution of the rainfall input in hydrological models must be in accordance with the catchment characteristics that determine its characteristic response time during a storm event (land cover, size, slopes, drainage network and

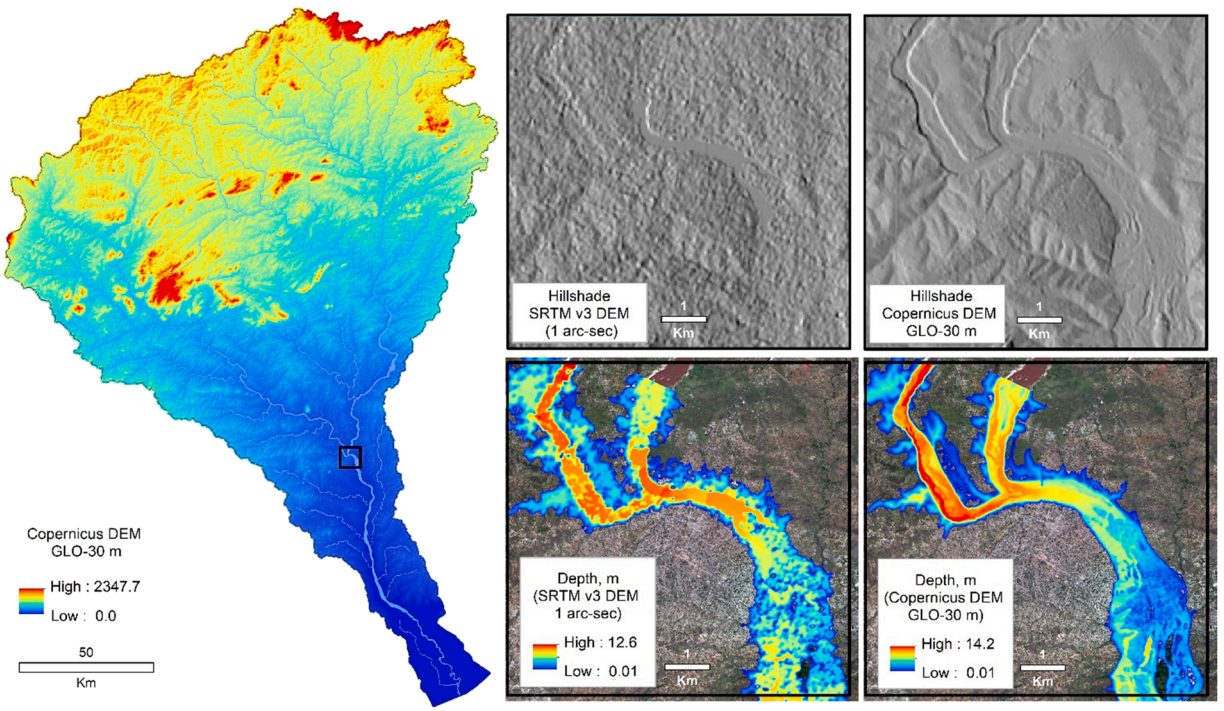

Fig. 2. Topography of the whole Licungo basin obtained from Copernicus GLO-30 DEM (left), and comparison of the topography and water depths in the confluence of the Licungo and Lugela rivers, obtained from SRTM v3 and Copernicus GLO-30 (right).

shape). In small catchments of a few km^2, a time resolution of 10–15 min and a spatial resolution of 1 km is usually needed. For larger catchments, over a thousand km^2, a time resolution of one hour and a spatial resolution of 10 km are generally sufficient.

Precipitation gauges still provide the most accurate point estimates of rainfall intensity. However, their practical application is limited due to the sparse spatial distribution of gauges over the majority of African countries. On the other hand, satellite rainfall estimates, although less accurate than rain gauge data, have an almost global coverage and provide valuable products for hydrological simulations in data-scarce regions (Liu et al., 2020).

In recent years several satellite missions providing satellite rainfall estimates (SRE) have become operational and their products are freely available. However, for most of these the temporal resolution is too low for use in flood inundation studies, being oriented towards water resources or climate change studies. For the evaluation of extreme floods, the following are worth mentioning: the Precipitation Estimation from Remotely Sensed Information using Artificial Neural Networks (PERSIANN) (Hsu and Sorooshian, 2008), the PERSIANN-CCS (Hong et al., 2004; Nguyen et al., 2018), the Global Satellite Mapping of Precipitation (GSMaP) (Kubota et al., 2007), the Tropical Rainfall Measuring Mission (TRMM) (Huffman et al., 2007) and the Global Precipitation Measurement (GPM) mission (Huffman et al., 2020).

The TRMM operated from 1997 to 2015, providing rainfall estimates between latitudes 35^{o}N and 35^{o}S with a time resolution of 3 h and a spatial resolution of 0.25^o (roughly 25 km) that have been used in many flood studies (Curtis et al., 2007; Harris et al., 2007; Komi et al., 2017; Li et al., 2009; Tekeli et al., 2016; Yang et al., 2017). The GPM mission is the follow-up to the TRMM that was launched in order to continue and improve upon satellite-based rainfall and snowfall observations on a global scale. The Level 3 Integrated Multi-Satellite Retrievals for GPM (IMERG) product provides precipitation estimates since March 2014 within the 60^o N–S latitude band, from the combined use of passive microwave (PMW) and infrared (IR) sensors. The GPM-IMERG data set is available in the form of near-real-time data divided into three different categories: near-real-time Early Run (ER) with a latency of 4 h;

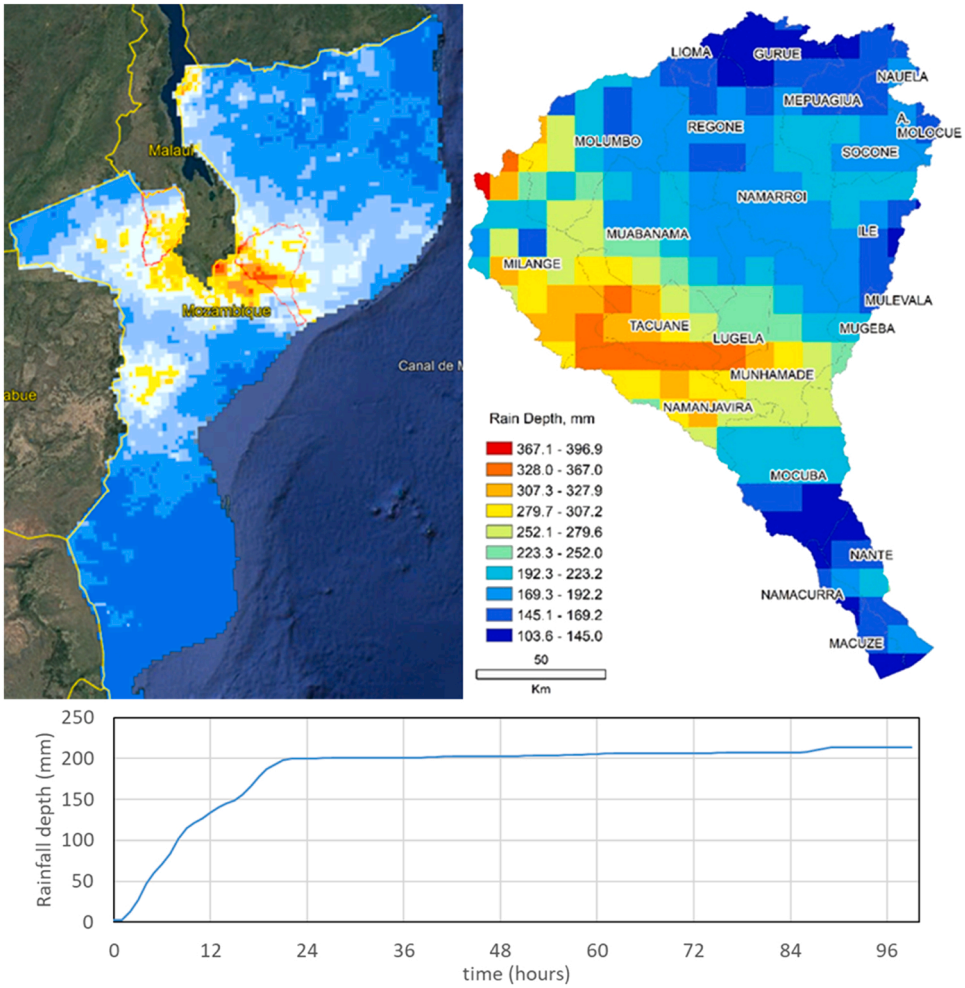

Fig. 3. Spatial distribution of rainfall depth in Mozambique (upper-left) and in the Licungo basin (upper-right) during TS Ana (24–27 January 2022), obtained from the GPM database, and the basin-averaged rainfall depth-duration curve (lower). Source of the background image on the left: Google earth V 7.3.4.8642. Imagery date: December 14, 2015. http://www.earth.google.com (Accessed June 26, 2022).

near-real-time reprocessed Late Run (LR) with a latency of 14 h; and Final Run (FR) with more precise precipitations estimates but with a higher latency of approximately 3–4 months. These products have a spatial resolution of 0.1° (roughly 10 km) and temporal resolutions of 30 min, 3 h, 1 day, 3 days, 7 days and 1 month. A comprehensive review of GPM-IMERG validation studies from 2016 to 2019 around the globe characterized by various locations, topography, and climatic regions can be found in Pradhan et al. (2022).

In the present study we used the GPM-IMERG Late Precipitation L3 Half Hourly 0.1° data set. The Licungo basin is covered by 236 rainfall pixels. The rainfall estimates during the simulation period (from 24/01/2022 at 00:00 until 28/01/2022 at 03:00) were retrieved (198 files) and used as the rainfall input for the numerical model. Fig. 3 shows the spatial distribution of rainfall depth in the Licungo basin during the simulation period, as well as the basin-averaged rainfall depth-duration curve, which shows that most of the rainfall (94 %) fall during the first 24 h.

3.1.3. Land cover

Land cover data are needed for flood estimation in order to characterize hydrological processes as flow resistance and evapotranspiration. There are several land cover data products available for free. In this study we have used the land cover maps developed by the European Space Agency (ESA) through the GlobCover project. Those maps were derived from the MERIS sensor observations on board the ENVISAT satellite mission during 2005–2006 and 2009, and they are provided globally at a resolution of 300 m. However, for this study we have used a prototype land cover product that was released only for Africa by the GlobCover project with a spatial resolution of 20 m, based on Sentinel-2A observations from December 2015 to December 2016 (Fig. 4). According to this land cover map, 47% of the basin is covered by trees, while cropland and grassland are the other two predominant land uses, covering 30 % and 20 % of the basin, respectively. These three land uses occupy 97 % of the basin's surface.

Two alternative land cover data sources that could also be used for our purposes are the Climate Change Initiative (CCI) Land Cover project from the ESA (ESA, 2017), which includes global land cover maps at 300 m spatial resolution on an annual basis since 1992, and the Terra and Aqua Combined Moderate Resolution Imaging Spectroradiometer (MODIS) Land Cover Type, which provides global land cover types at yearly intervals (2001–2018) with a spatial resolution of 500 m.

3.1.4. Infiltration

Infiltration, together with rainfall, is one of the most important processes in the generation of floods. The infiltration capacity of the terrain depends mainly on the soil type, land cover, slope and moisture content. From the many formulations available, the Soil

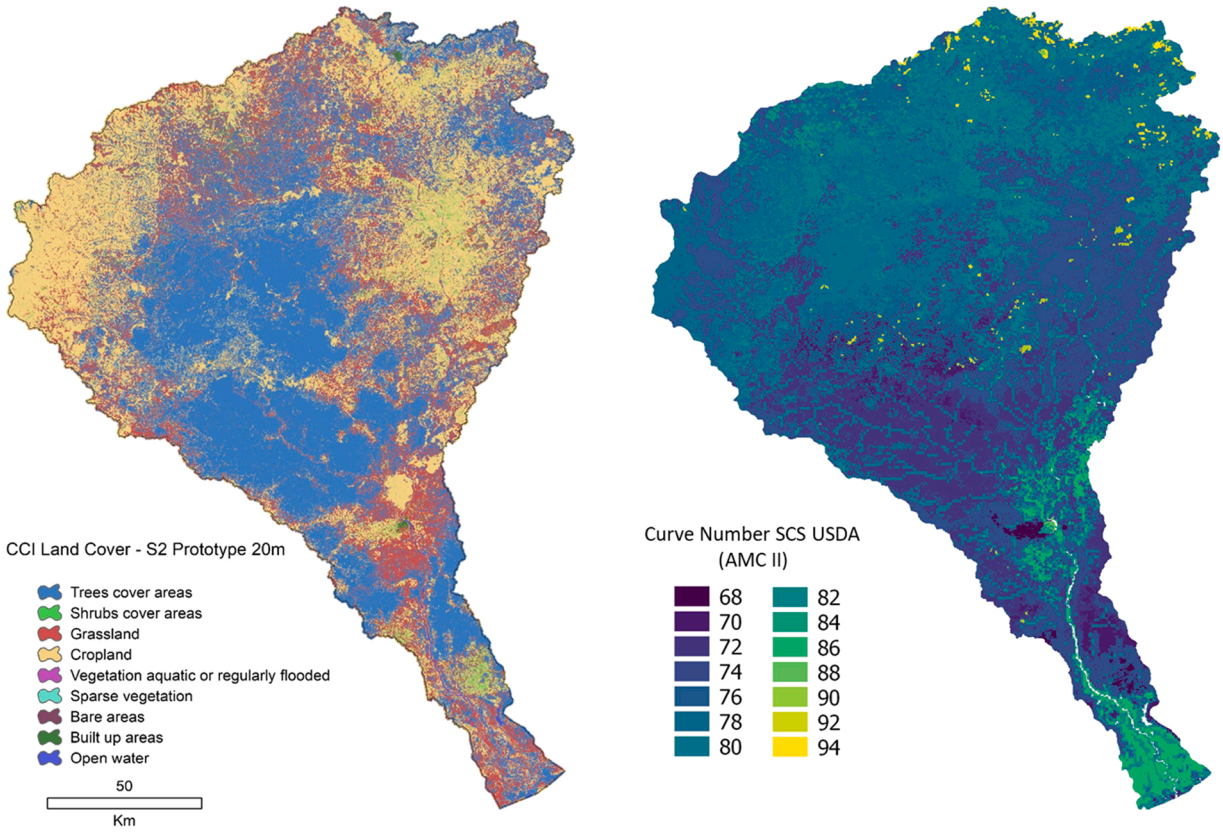

Fig. 4. Spatial distribution of land uses obtained from the ESA CCI Land Cover project (left) and CN obtained from GCN250 (Jaafar et al., 2019), in the whole Licungo basin.

Conservation Service Curve Number (SCS-CN) is among the most widely used for the estimation of infiltration losses in flood studies. It characterizes the infiltration capacity of the soil using a single parameter, the curve number (CN), this having been extensively tabulated as a function of the hydrological soil group, the land cover and the terrain slope (Mishra and Singh, 2003). Corrections due to antecedent soil moisture condition (AMC) can also be considered, but these are difficult to calibrate in the absence of discharge field data and might be dependent on the study region. In fact, several studies have pointed out the limitations of the standard corrections used to correct the CN as a function of the 5-day antecedent rainfall, and have recognized that, in order to account properly for the AMC effect on the SCS-CN method, more sophisticated approaches should be implemented that are difficult to apply when no observed data are available (see, for instance, Caletka et al., 2020, Cea and Fraga, 2018, Hope and Schulze, 1982, Huang et al., 2007, Shi and Wang, 2020, Soulis, 2021).

The land cover and the terrain slope can easily be derived from any of the GDEMs and land cover maps mentioned in Sections 3.1.1 and 3.1.2. The hydrological soil groups can be obtained with a resolution of 250 m from the HYSOGs250m global data set (Ross et al., 2018). The HYSOGs250m data set were derived from soil texture classes and depth to bedrock data provided by the FAO Harmonized World Soil Database, in order to support SCS-CN runoff modelling at regional and continental scales, and hence are especially suitable for the estimation of the CN.

In this study we have used the global CN estimation GCN250, presented recently by Jaafar et al. (2019), which is based on the hydrological soil groups from the HYSOG250m data set and on the land cover classification of 2015 from the ESA CCI Land Cover project. The GCN250 data set has a spatial resolution of 250 m and is provided for average, dry, and wet antecedent soil moisture conditions. According to this data set, the CN in the Licungo basin varies between 59 and 98, with a basin-averaged value of 77, a mode of 79 and a median of 78.

3.1.5. Flood extent

Earth observation data from space can be used to estimate the extent of floods associated with extreme rainfall events in large and inaccessible territories, as is the case with floods caused by tropical cyclones in Mozambique. This information can then be used to assess economic damages, quantify the exposed population, and define evacuation routes. An observed estimate of the flood extent can also be very valuable for the validation of hydrological and hydraulic models in data-scarce regions (Di Baldassarre et al., 2009; Domeneghetti et al., 2014; Schumann and Moller, 2015; Sun et al., 2012).

The ESA satellites Sentinel-1, Sentinel-2 and Sentinel-3 provide images that can be used during the different phases of a flood management plan (Kuntla and Manjusree, 2021). Sentinel-1A is equipped with a C-band Advanced Synthetic Aperture Radar with a pixel spacing of 10 m, and processed to Level-1 Ground Range Detected with High-resolution (GRDH). One of the biggest advantages of using SAR measurements over optical imagery for flood mapping is that SAR is not limited by the presence of clouds, and is able to

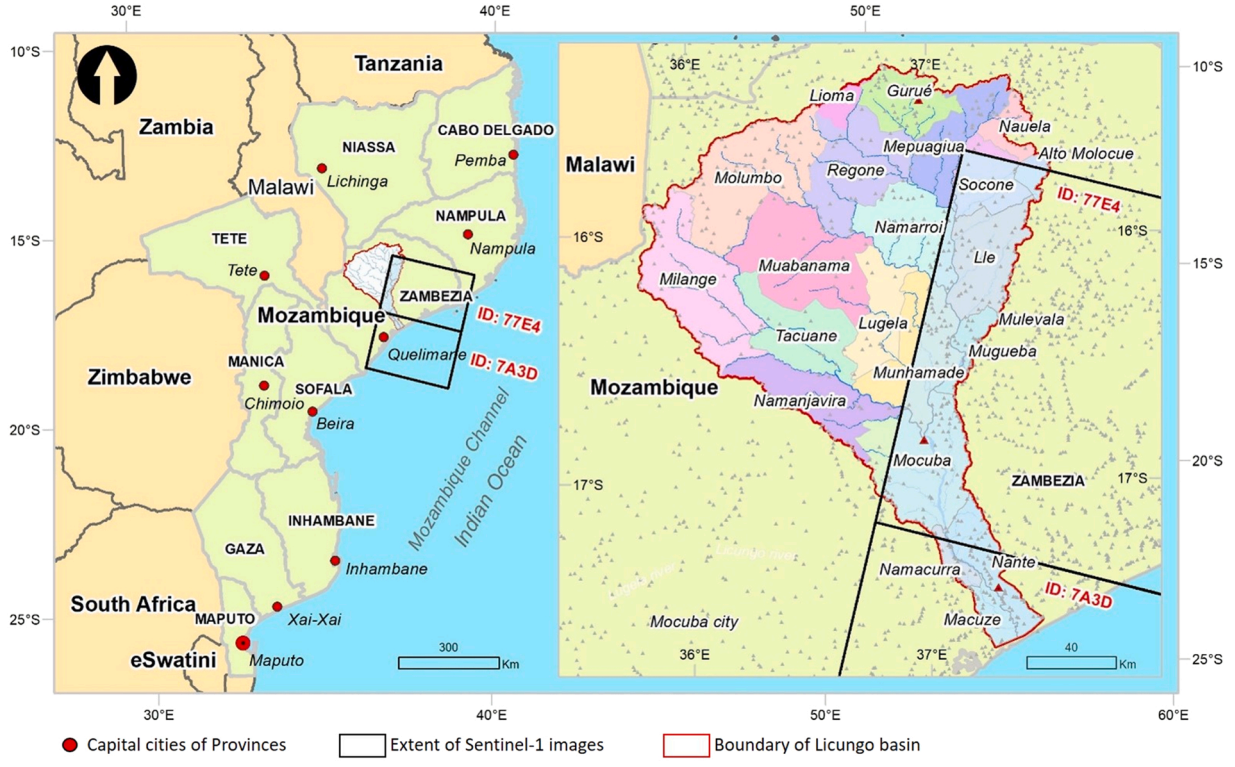

Fig. 5. Coverage of S-1A SAR-C products ID 77E4 and 7A3D over the Licungo basin on 28/01/2022.

effectively capture images during rain and other adverse weather conditions, both day and night. In SAR imagery water appears to be dark due to the low backscatter from its smooth surface, whereas the surrounding terrain appears bright due to its roughness that causes moderate backscatter (Kuntla and Manjusree, 2020). Sentinel-1 imagery is the base of the dashboard *UNOSAT S-1 FloodAI Monitoring Dashboard*, which is managed by the United Nations Satellite Centre (UNOSAT) for the analysis of the flood exposed population in several countries of Africa and Asia, including Mozambique (Nemni et al., 2020).

In the present study the flood extent over the Licungo basin was estimated using the Sentinel Application Platform (SNAP) Toolkit developed by ESA for processing SAR-C images (Zuhlke et al., 2015). This process was done following a standardised procedure to process Level-1 GRDH products in order to obtain final sigma nought images and interferograms corresponding to the flood extent.

The only two available images from ESA during TS Ana are those taken by Sentinel-1A on 28/01/2022 at 03:00 UTC, which cover partially the Licungo basin (Fig. 5). The area covered by the two images is limited to the east part of the basin, and it only represents 28 % (6415 km^2) of the catchment area. Nonetheless, the images cover the APs of Mocuba, Nante, Namacurra and Macuze, which are the locations that include most of the flood prone areas in the basin, and where most of the population is concentrated.

3.1.6. Population maps

In order to estimate the number of people exposed to a storm event, it is necessary to know the spatial distribution of population in the flooded areas. Population maps, in combination with flood extent maps, can be used here. Global gridded population data sets provide estimates of population figures in a uniform grid across the world, contributing to a better understanding of where groups of people are settled (Leyk et al., 2019). There are currently several global population data sets that can be used for this purpose, such as the Gridded Population of the World (GPW), the Global Human Settlement Layer-Population (GHS-POP), the LandScan Global Population Database (LandScan Global), the World Population Estimate (WPE), the High-Resolution Settlement Layer (HRSL), and the WorldPop. A detailed description can be found in Leyk et al. (2019) and Dahmm et al. (2020).

In this study we used the WorldPop gridded population data set (Tatem, 2017; WorldPop et al., 2018), which is freely available for the whole world with a spatial resolution of 3 arc-sec (roughly 90 m). It was derived using a Random Forest model to produce a predictive weighting layer for asymetrically redistributing population counts into gridded cells (Stevens et al., 2015). One of strengths of WorldPop is that it offers population estimates every year since 2000, which makes it comparable over time and facilitates the monitoring of population evolution. In the case of Mozambique, the latest available estimate is for 2020, which was the one used in this

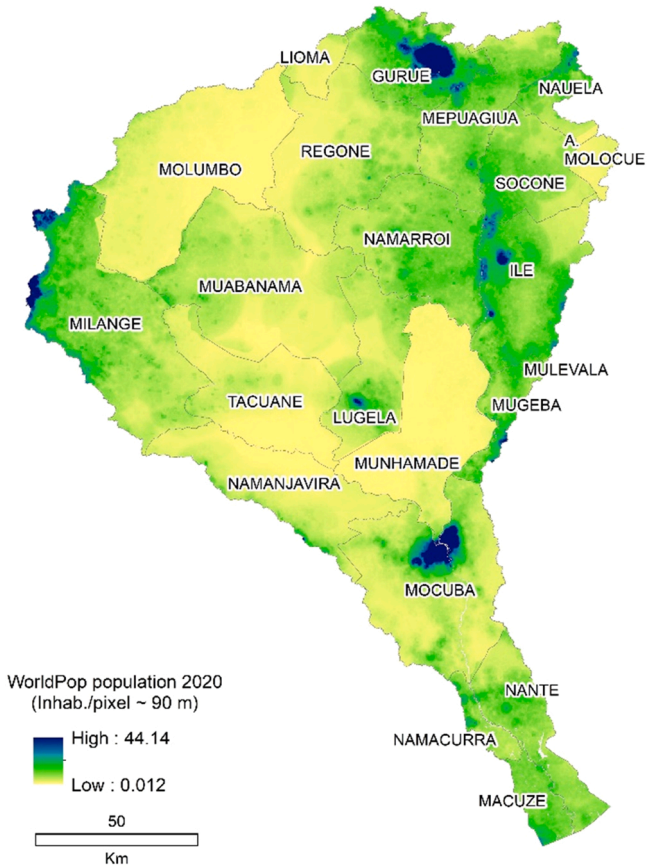

Fig. 6. WorldPop population density (inhabitants per pixel of 90 m width) estimate for 2020 in Mozambique.

study (Fig. 6).

3.2. Integrated hydrological-hydraulic modelling

There are several modelling approaches that can be used to evaluate flood hazard (Cea and Costabile, 2022; Teng et al., 2017). In large catchments the standard two-stage approach consists of using a hydrological model first to transform rainfall fields into water discharges along the main river network, and then using those discharges as the input for a detailed hydraulic model to compute the extent of the inundation, water depths and velocities only at specific flood prone river reaches, the so-called Areas of Potential Significant Flood Risk (APSFR). The rainfall-discharge transformation can be done with a lumped, semi-distributed or fully-distributed hydrological model, while the local hydraulic modelling in the APSFR is often performed with a 2D depth-averaged shallow water model, although other configurations are possible.

Recently, different integrated modelling approaches have been proposed in which the rainfall-runoff transformation in the whole catchment and the flood inundation in the river network are computed simultaneously (Khaing et al., 2019; Sanz-Ramos et al., 2021; Xia et al., 2019). With these integrated approaches there is a continuous spatially distributed contribution of surface runoff to the river streams and over the APSFR, which is a far better representation of reality than the classical two-stage approach. In addition, an integrated hydrological/hydraulic modelling approach has the advantage of providing a global estimate of inundation in the entire catchment and river network with just one simulation. The main drawback of such approaches is the different spatial scales involved in the modelling of an entire catchment, including hillslope runoff and river flow. This implies the use of discretisation grids with a very large number of elements, requiring enhanced computational performance of the numerical solver. For instance, Xia et al. (2019) presented an integrated simulation of a flood event in a 2500 km^2 catchment in which the 2D-SWEs were solved in a uniform structured grid with 100 million computational cells (element size of 25 m^2). Such a modelling approach required a multi-GPU parallelization scheme and the use of 8 Nvidia Tesla K80 GPUs in order to obtain a computational time 2.5 times faster than real time. This means that the same modelling approach, applied to a four-day event in the Licungo catchment (23,263 km^2), would require over two weeks of computational time, using eight high-performance GPUs and a very complex High Performance Computing implementation. In addition, such a spatial resolution would need to handle a mesh of one billion elements. This is very far from being affordable for most inundation studies in developing countries, and thus the computational requirements must be relaxed for practical purposes.

In this study we have used an integrated modelling approach based on solving the 2D-SWE in the whole catchment, using an unstructured computational mesh with a lower spatial resolution than Xia et al. (2019), given the far larger size of the Licungo basin (23,263 km^2). The advantage of using an unstructured mesh is that the grid can be adapted to the catchment morphology, using different element sizes in the hillslopes and in the river network, where the flow concentrates. In our case study we have used triangular elements with edge sizes ranging from 30 m in some river reaches to 140 m in the hillslopes. To this end, the river network width was digitized manually from an ortophoto obtained from Sentinel-2, obtaining the main river channels, as shown in Fig. 7. A similar procedure to define the river network width was followed by Komi et al. (2017). Alternatively, the definition of the river width can also be done based on the contributing drainage area (CDA) at each river cross section. This, for instance, is done by Neal et al. (2012) using the empirical hydraulic-morphological relationships proposed by Leopold and Maddock (1953), or by Uber et al. (2021) based on visual inspection of the river network at cross sections with different CDAs. However, for the purposes of the present case study, we considered digitization from a visual inspection of the ortophoto, although more laborious, to be the most appropriate approach. This zonification produced a river network with a total length of 700 km and a surface of 331 km^2 (Fig. 7). With this geometry and mesh configuration, the 331 km^2 of main channels were discretised with approximately 0.3 million elements, while 2.9

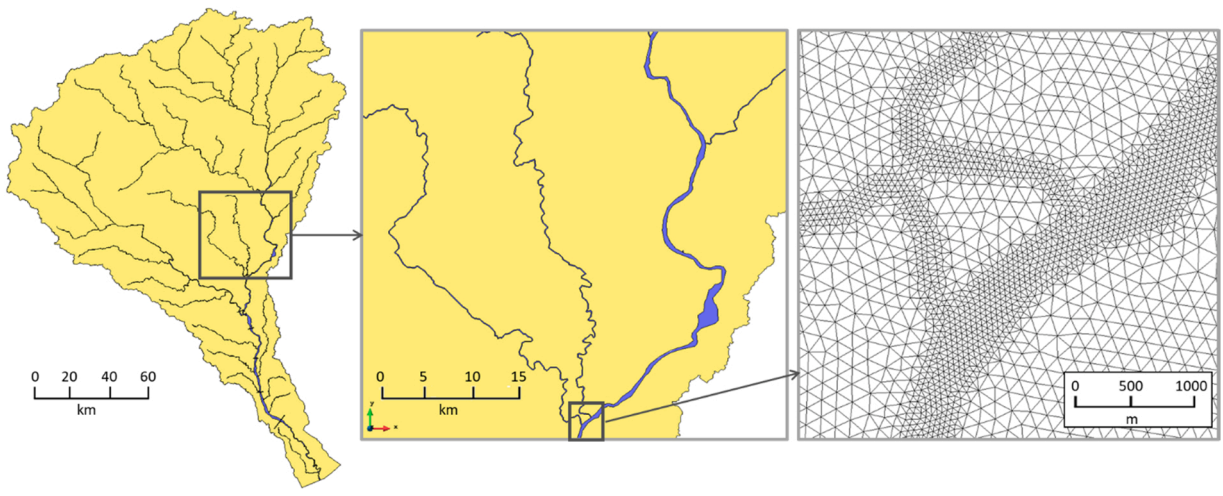

Fig. 7. Numerical discretisation of the Licungo basin.

million elements were used to discretise the floodplains and hillslopes, which occupy an area of 22,932 km^2. The total number of elements of the mesh was 3.2 million.

The 2D-SWEs were solved with the numerical model Iber+ (García-Feal et al., 2018), which is a GPU-parallelized implementation of the software Iber (Bladé et al., 2014), and is available free of cost at www.iberaula.com. The equations solved by the model can be expressed as:

$$\frac{\partial h}{\partial t} + \frac{\partial q_x}{\partial x} + \frac{\partial q_y}{\partial y} = R - i \tag{1}$$

$$\frac{\partial q_x}{\partial t} + \frac{\partial}{\partial x}\left(\frac{q_x^2}{h} + g\frac{h^2}{2}\right) + \frac{\partial}{\partial y}\left(\frac{q_x q_y}{h}\right) = -gh\frac{\partial z_b}{\partial x} - g\frac{n^2}{h^{7/3}}|q|q_x \tag{2}$$

$$\frac{\partial q_y}{\partial t} + \frac{\partial}{\partial x}\left(\frac{q_x q_y}{h}\right) + \frac{\partial}{\partial y}\left(\frac{q_y^2}{h} + g\frac{h^2}{2}\right) = -gh\frac{\partial z_b}{\partial y} - g\frac{n^2}{h^{7/3}}|q|q_y \tag{3}$$

where h is the water depth, q_x, q_y and $|q|$ are the two components of the unit discharge and its modulus, z_b is the bed elevation, n is the Manning coefficient, g is the gravity acceleration, R is the rainfall intensity, and i is the infiltration rate. All the input data and parameters (rainfall fields, infiltration parameters and Manning coefficient) can vary in space.

Iber implements an unstructured finite volume solver for the 2D-SWEs. It was initially developed to model river flow, but in recent years several numerical implementations have broadened its range of application to hydrological processes (Cea and Blade, 2015), allowing the simulation of rainfall-runoff transformation and river inundation processes simultaneously. The model has previously been applied and validated in rainfall-runoff computations at different spatial scales (Cea et al., 2016; Cea and Blade, 2015; Fraga et al., 2019; Sanz-Ramos et al., 2018; Sanz-Ramos et al., 2021; Tamagnone et al., 2020; Uber et al., 2021), and its reliability and computational efficiency has led to its implementation in several flood early warning systems (Fernández-Nóvoa et al., 2020; Fraga et al., 2020; González-Cao et al., 2019).

As mentioned in Section 3.1.4, the soil infiltration capacity was modelled with the SCS-CN method, using the spatial distribution of CN provided by Jaafar et al. (2019) for normal antecedent soil moisture conditions (Fig. 4). In order to define the Manning's coefficient, six different land covers were considered (Trees, Shrubs, Grassland, Cropland, Built-up areas, and Rivers). Their spatial distribution over the hillslopes and floodplains was retrieved from the high-resolution land cover map provided by the ESA CCI project for Africa at 20 m resolution, previously mentioned in Section 3.1.3 and shown in Fig. 4, except for the Rivers land cover, which was defined manually for the whole stream network, as shown in Fig. 7, since the Open Water cover defined in the ESA CCI map does not include a precise definition of the whole river network. For modelling purposes, the Manning coefficients defined in Table 2 were assigned to each land use (Fig. 8).

Rainfall was defined in the model as raster files of precipitation intensity obtained from the GPM database, as detailed in Section 3.1.2, with a spatial and temporal resolutions of 10 km and 30 min, respectively. The simulated period is from 24/01/2022 at 00:00, the time at which the TC Ana hit the Licungo basin, until 28/01/2022 at 03:00, the time at which the Sentinel-1 image used to estimate the flood extent was taken. As shown in Fig. 3, most of the rainfall (94 %) took place in the first 24 h.

With the numerical setup described above it took around 1 h of computational time to model the whole simulation period of 4.1 days (i.e., 100 times faster than real time), using a standard laptop with a NVIDIA GeForce RTX 3080 Ti, which is an affordable hardware configuration.

3.3. Flood extent-based performance indices

The predictive capacity of the numerical model in the Licungo catchment was assessed by comparing the water extent, computed numerically, with the one estimated from the Sentinel-1 image taken on 28/01/2022 at 03:00. This image was processed as described in Section 3.1.5 in order to obtain a raster with the observed flood extent, with a spatial resolution of 10 m. This raster was compared, on a pixel basis, with the prediction obtained using Iber for the same date and time. To do so, the flood extent in Iber was defined as the envelope of the wet mesh elements, and the water depths computed within the flood extent were transferred from the triangular elements to the centre of the pixels using a linear interpolation scheme.

To quantify the agreement between both inundation maps, the following indices were computed: 1) Hit Rate (proportion of the area

Table 2
Manning coefficient assigned to each land use considered in the ESA CCI Land Cover map.

Land use	Manning (s.m$^{-1/3}$)
Trees	0.070
Shrubs	0.060
Grassland	0.035
Cropland	0.050
Built-up areas	0.100
River	0.040

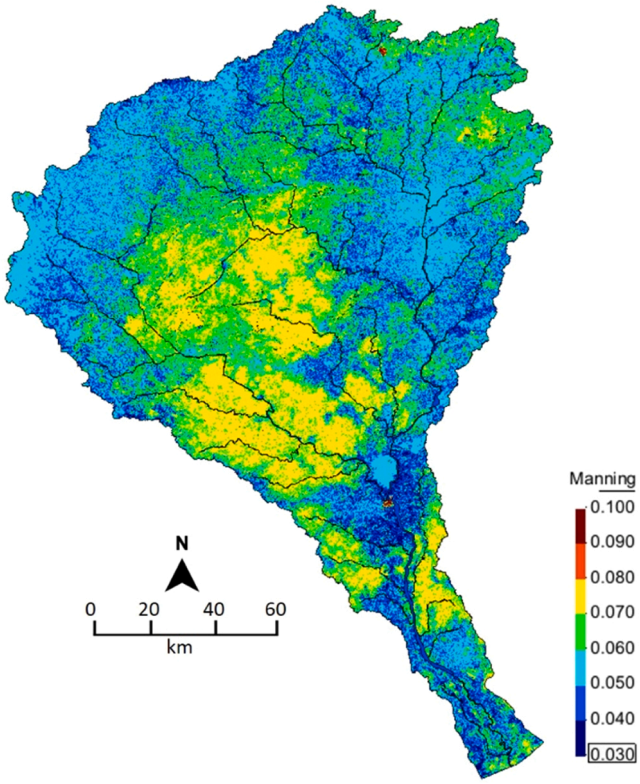

Fig. 8. Spatial distribution of the Manning's coefficient used in Iber.

observed as flooded that the model also predicts as flooded); 2) False Alarm Ratio (proportion of the area predicted as flooded by the model that has been classified as dry by the observation); 3) Bias (ratio of the area predicted as flooded and the area observed as flooded); and 4) F_1 score (combination of the Hit Rate and False Alarm Ratio in a single performance measure that varies between 0 and 1). These indices were computed as:

$$HR = \frac{TP}{TP+FN} \quad FAR = \frac{FP}{TP+FP} \quad Bias = \frac{TP+FP}{TP+FN} \quad F_1 = 2\frac{HR \quad (1-FAR)}{HR+(1-FAR)}$$

where *HR* is the Hit Rate, *FAR* is the False Alarm Ratio, *TP* are the true positives (number of grid cells correctly predicted as flooded), *FP* are the false positives (number of cells that the model predicted as flooded but were observed as dry) and *FN* are the false negatives (number of cells predicted as dry but observed as flooded) (Table 3). The *HR* and F_1 score vary between 0 (worst performance) and 1 (best performance). The *FAR* varies between 0 (best performance) and 1 (worst performance). The *Bias* varies between 0 and infinite. If $Bias = 1$, the modelled and observed flooded areas are equal. If $Bias < 1$, the model underestimates the flood extent. If $Bias > 1$, the model overestimates the flood extent.

This kind of cell-by-cell performance indices are commonly used in the comparison of 2D models with field observations (Bennett et al., 2013; Bermúdez et al., 2019; Costabile et al., 2020; Falter et al., 2013; Grimaldi et al., 2016).

The performance indices were evaluated both within the region of the Licungo basin covered by the Sentinel-1 images, and at the reach scale in three river reaches with lengths from 15 to 25 km, including their associated floodplains (Fig. 1). Reach 1 is located at the confluence between the rivers Lugela (right tributary) and Licungo (left tributary), around the city of Mocuba, and has a meandering morphology. Reach 2 is rather straight and confined, and is located approximately 20 km downstream from Reach 1. Both reaches have a length of approximately 15 km. Reach 3 is the longest (around 25 km), is located near the basin outlet, and has a relatively flat topography with a braided morphology. These three reaches were chosen because they represent different river morphologies and are

Table 3
Contingency table for the evaluation of water depth predictions. A pixel is considered to be predicted as flooded if the water depth computed by the numerical model is greater than 0.10 m.

	Observed as flooded	Observed as dry
Predicted as flooded	TP (true positive)	FP (False positive)
Predicted as dry	FN (False negative)	TN (True negative)

located in Administrative Posts with a high number of people exposed to flooding, as will be shown in the following sections. For ease of reference, and as opposed to *reach scale*, we will refer to the comparison within the region covered by the Sentinel-1 images as *catchment scale*, even if it does not cover the whole Licungo basin.

4. Results and discussion

4.1. Flood extent and validation

Tropical Strom Ana hit the Licungo basin on 24/01/2022 at 00:00, leaving a basin-averaged rainfall depth of 213 mm, most of which fell within the first 24 h (Fig. 3). The rainfall depth at certain locations on the west part of the basin reached values of around 350 mm. The only available observed data that can be used to estimate the extent of the flood is the image taken by Sentinel-1 on 28/01/2022 at 03:00 (Fig. 5). This image covers only the east part of the basin and was taken 4 days after the start of the storm, with the flood in its recession period. Thus, the flooded area observed is much smaller than the maximum flood extent during the storm event. Fig. 9 shows the flooded area estimated from Sentinel-1, as well as the area computed with Iber at the same time, assuming in the latter case that the flooded areas are those with a water depth greater than 0.1 m. A water depth threshold is needed to define the flood extent in the numerical model for two reasons. First, because the model input is rainfall and thus there is a positive water depth for almost every computational cell. Second, because very small water depths will not be classified as flooded in the analysis of the satellite image. The specific threshold chosen (0.1 m) might have an effect on the results, but it has been verified that the analysis and conclusions based on the performance measures presented below do indeed hold for thresholds between 0.05 and 0.20 m. Thresholds of the same order of magnitude have been used in other studies (Eilander et al., 2022; Wing et al., 2017).

Table 4 shows the flood extent-based performance measures computed from the comparison of the satellite image and the prediction of Iber. The *Sentinel-1 coverage* column includes the performance scores computed for the whole area covered by the Sentinel-1 image within the Licungo basin (red contour in Fig. 9), that is, at the catchment scale. At this scale the *HR* is quite high (0.79), meaning that most of the observed flooded area is captured by the model. On the other hand, at the catchment scale the model predicts a lot of flooded areas that are not identified in the satellite image, and would therefore be classified as False Positives. Thus, the *FAR* and the *Bias* are quite high (0.60 and 0.53, respectively). Nevertheless, the values of the *FAR* and *Bias* at the catchment scale should be taken with caution, since most of the False Positives lie in the hillslopes or in tributaries of the Licungo and Lugela rivers that are not captured by the analysis of the satellite image, as clearly seen in Fig. 10. With the flood still in its recession phase, all those tributaries that are captured by Iber (red areas in Fig. 10) should be conveying a significant amount of water, although they are not identified as flooded areas in the analysis of the satellite image (blue areas in Fig. 10). Thus, the water extension predicted by Iber in all those small tributaries is contributing to the number of False Positives when computing the *FAR* and *Bias*, which explains the high value of these performance measures when computed at the catchment scale. The limitations of using SAR images to derive flood extent maps have been analysed in recent studies which point out the importance of defining exclusion maps that identify the pixels in which the satellite-derived estimation is not reliable, this in order to avoid a substantial reduction in the performance measures of hydrological models (Zhao et al., 2021; Di Mauro et al., 2021). In our case, the most likely reason why the satellite-derived map fails to capture the water extent in the tributaries is the presence of riparian vegetation that masks the water in and around small rivers. The presence of sand bars and braided streams at some locations also contributes to the difficulty of identifying some narrow tributaries. Moreover, the

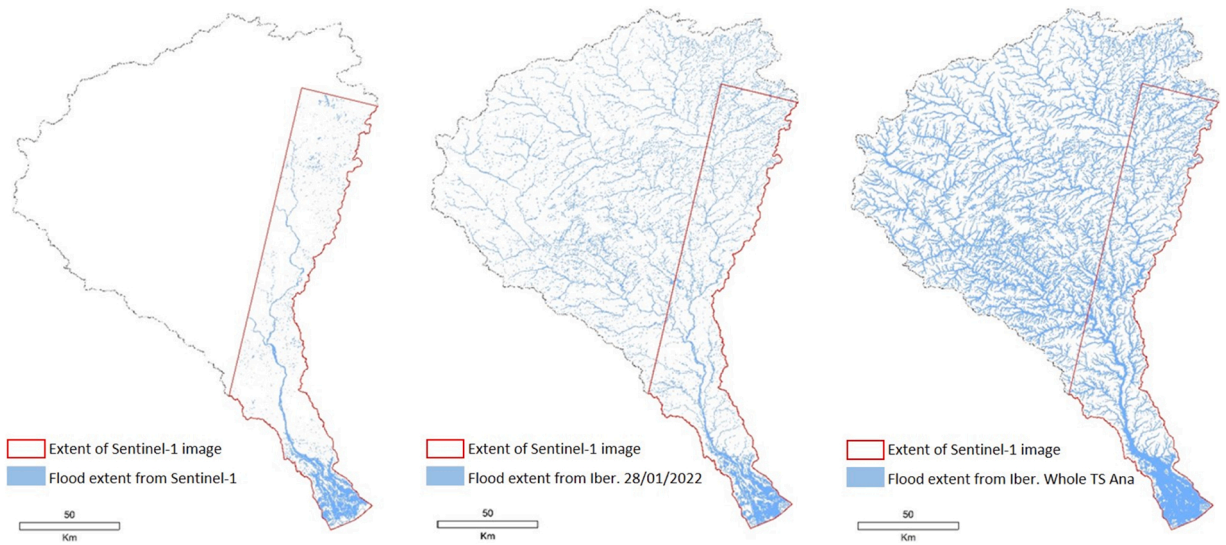

Fig. 9. Flood extent on the Licungo basin, estimated from Sentinel-1 on 28/01/2022 at 03:00 (left), computed with Iber as the area with $h > 0.1$ m on 28/01/2022 at 03:00 (middle) and computed with Iber as the area with $h > 0.1$ m for the whole TS Ana event (right).

Table 4
Flood extent-based performance measures computed for three different river reaches and for the whole area covered by Sentinel-1 on 28/01/2022 at 03:00. **FAR* and *Bias* for the whole Sentinel-1 coverage should be taken with caution for the reasons noted in the text.

Score	Units	Sentinel-1 coverage	Reach 1	Reach 2	Reach 3
TP (True Positives)	km^2	260.85	6.60	6.42	29.43
FP (False Positives)	km^2	385.30	1.85	0.82	13.44
FN (False Negatives)	km^2	69.82	1.38	1.01	9.35
TP + FP (Predicted flood extent)	km^2	646.15	8.45	7.24	42.87
TP + FN (Observed flood extent)	km^2	330.67	7.99	7.43	38.78
HR	–	**0.79**	**0.83**	**0.86**	**0.76**
FAR	–	**0.60***	**0.22**	**0.11**	**0.31**
F_1	–	**0.53**	**0.80**	**0.88**	**0.72**
Bias	–	**0.53***	**0.03**	**-0.01**	**0.06**

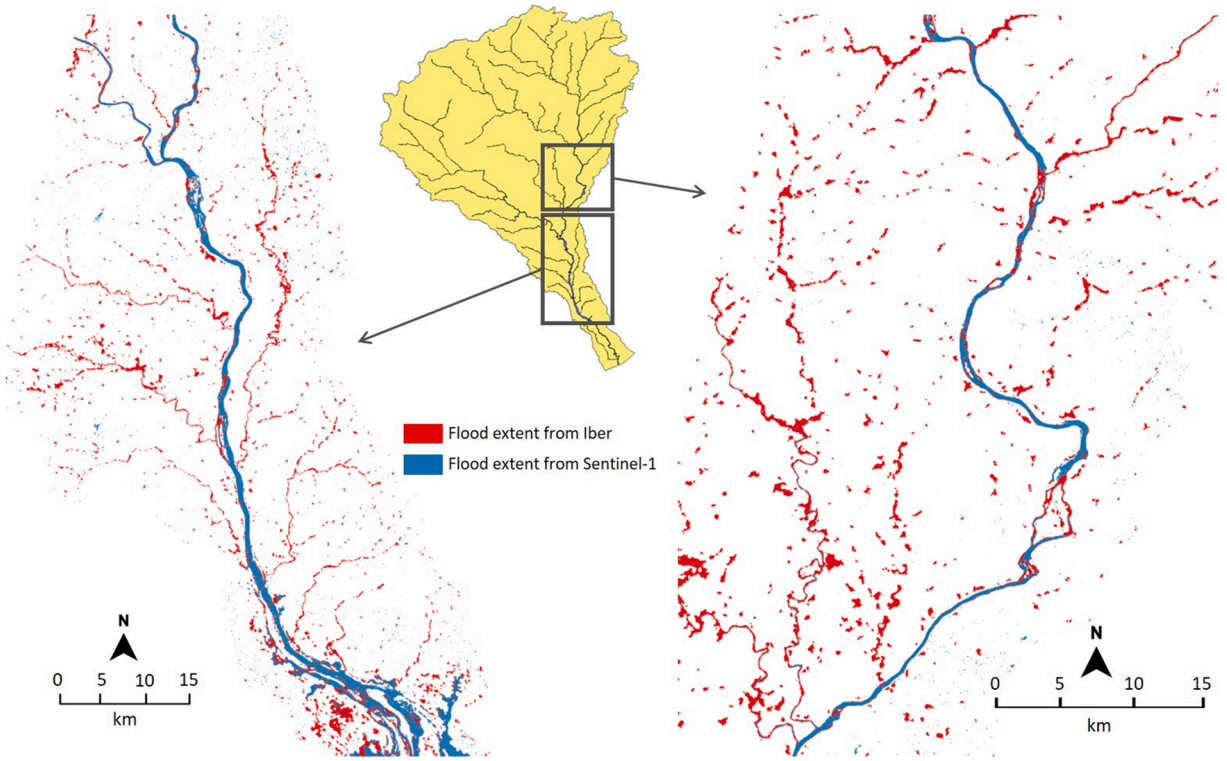

Fig. 10. Details of the flood extent on two areas of the Licungo basin on 28/01/2022 at 03:00, estimated from Sentinel-1 (blue) and computed with Iber as the area with h > 0.1 m (red).

fact that the width of the water table in many of these tributaries is equivalent to a few pixels in the satellite image also hinders their identification as flooded areas.

A second possible explanation of the high values of the *FAR* and *Bias* computed for the whole Sentinel-1 coverage is that the propagation of surface runoff in the numerical model creates local and isolated areas with water depths greater than 0.10 m that are not identified as flooded in the Sentinel-1 image (Fig. 10). The existence and extension of these isolated flooded areas is very much dependant on the local topography, and thus in the quality of the DEM, as well as on the water depth threshold used to define the flood extension in Iber (0.10 m). Increasing the water depth threshold diminishes the number of False Positives but also reduces the number of True Positives. Therefore, it was maintained at 0.10 m.

In order to explore the performance of the model at the reach scale, three river reaches with lengths varying from 15 to 25 km and different morphology were also analysed. The location of the reaches is shown in Fig. 1, and their description was provided above in Section 3.4. The overlapping between the flood extent computed with Iber and estimated from Sentinel-1 is much higher at the reach scale than at the catchment scale. The *HR* computed at reaches 1 and 2 is only slightly better than at the catchment scale (Table 4), but the *FAR* is far lower and the *Bias* is almost zero, meaning that at the reach scales there is not a significant overprediction of the flood extent. The performance measures computed at Reach 3 are not as good as in the other two reaches, but is still far better than at the catchment scale. This is due to the braided configuration of Reach 3, which makes the water depth results very dependent on the

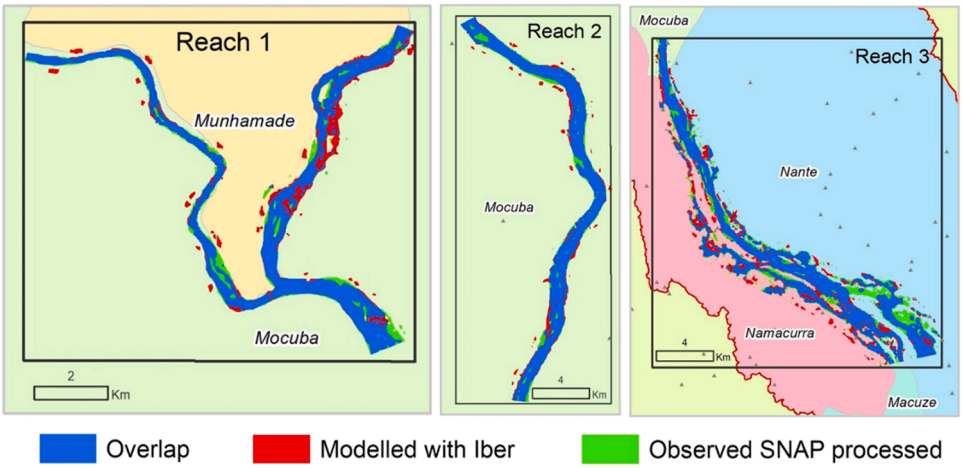

Fig. 11. Location of the three river reaches used to validate the flood-extent results (upper) and overlapping between the modelled and observed flood-extent on those three reaches on 28/01/2022 at 03:00 (lower).

accuracy and spatial resolution of the DEM.

From the above results we can conclude that the flood extent predicted by the numerical model is very reliable in the main river reaches and associated floodplains. At the basin scale it is difficult to assess the performance of the model because the satellite data do not provide a reliable estimate of the water extent in most of the tributaries of the main river streams. It seems that the model tends to overpredict the flood extent due to the presence of small and isolated flooded areas, but it is difficult to give precise and reliable performance measures.

4.2. Estimation of the population affected by TS Ana from satellite imagery

Fig. 12 and Table 5 show the estimates of the population exposed to flooding on 28/01/2022 at 03:00, obtained from overlying the WorldPop raster and the flood extent obtained from Sentinel-1. The data were aggregated by Administrative Posts (AP), the smallest administrative unit in Mozambique, and are presented as the total number of people exposed in each AP, and as the percentage of people exposed in each AP within the area covered by the Sentinel-1 image. The estimate obtained from Iber at the same date and time is also presented, for comparison and validation purposes.

According to the estimate obtained from Sentinel-1, more than 33,000 people were exposed to flooding at that time, from a total of 569,000 people living within the area covered by Sentinel-1 (Table 5). This is approximately 6 % of the population covered by the satellite image. In the APs located in the lower part of the basin, the percentage of people exposed was far higher, reaching values of 35 % in Macuze (Fig. 12 and Table 5). In this part of the basin, the higher discharges in combination with a relatively flat topography and a braided river morphology lead to large flooded areas, most of which are urbanised. These figures probably underestimate the population that was actually exposed to flooding at that time and in that region, since the satellite image does not identify as flooded most of the small tributaries of the Licungo, as discussed in the previous section and shown in Fig. 10.

Comparing the estimates obtained from the satellite image with those from Iber at the same time, the numerical model clearly predicts a far greater population exposed to flooding, with an overall overestimation factor of 1.6 between Iber and Sentinel-1. This factor should not be taken directly as a modelling error at the basin scale for the reasons already mentioned. The agreement between the satellite and numerical estimates is better in the APs located near the outlet of the catchment (Macuze, Nante, Namacurra and Mocuba), where the overestimation factors vary between 1.2 and 1.4, and deteriorates progressively as we move northwards, with overestimation factors between 1.4 and 3.0 in the APs of Munhamade, Mugeba and Namarroi, and greater than 3 in the northernmost APs (Ile, A. Molocue and Socone). This spatial pattern on the agreement between Iber and Sentinel-1 is clearly related to the configuration of the stream network and with the spatial resolution of the numerical model. While in the southern catchment there is one single main channel that is well defined and resolved in the numerical model, the stream network in the northern part is very ramified and consists of multiple headwater catchments with small tributaries that are not so accurately defined with the spatial resolution of the numerical mesh and DEM (Fig. 9). Added to this is the fact that the reliability of the flood extent estimate done from Sentinel-1 is more reliable in large and confined streams than in small intermittent and braided tributaries.

4.3. Estimation of the population affected by TS Ana from hydrological-hydraulic modelling

The comparative analysis of the flood extent presented in the previous sections was done on 28/01/2022 at 03:00, because it is the only time at which there is a satellite image available. However, at that time the flood was already receding, so the percentage of people affected during the entire TS Ana event was far greater. In addition, the satellite image only covers 28% of the catchment surface, so the total population exposed in the whole basin was even larger.

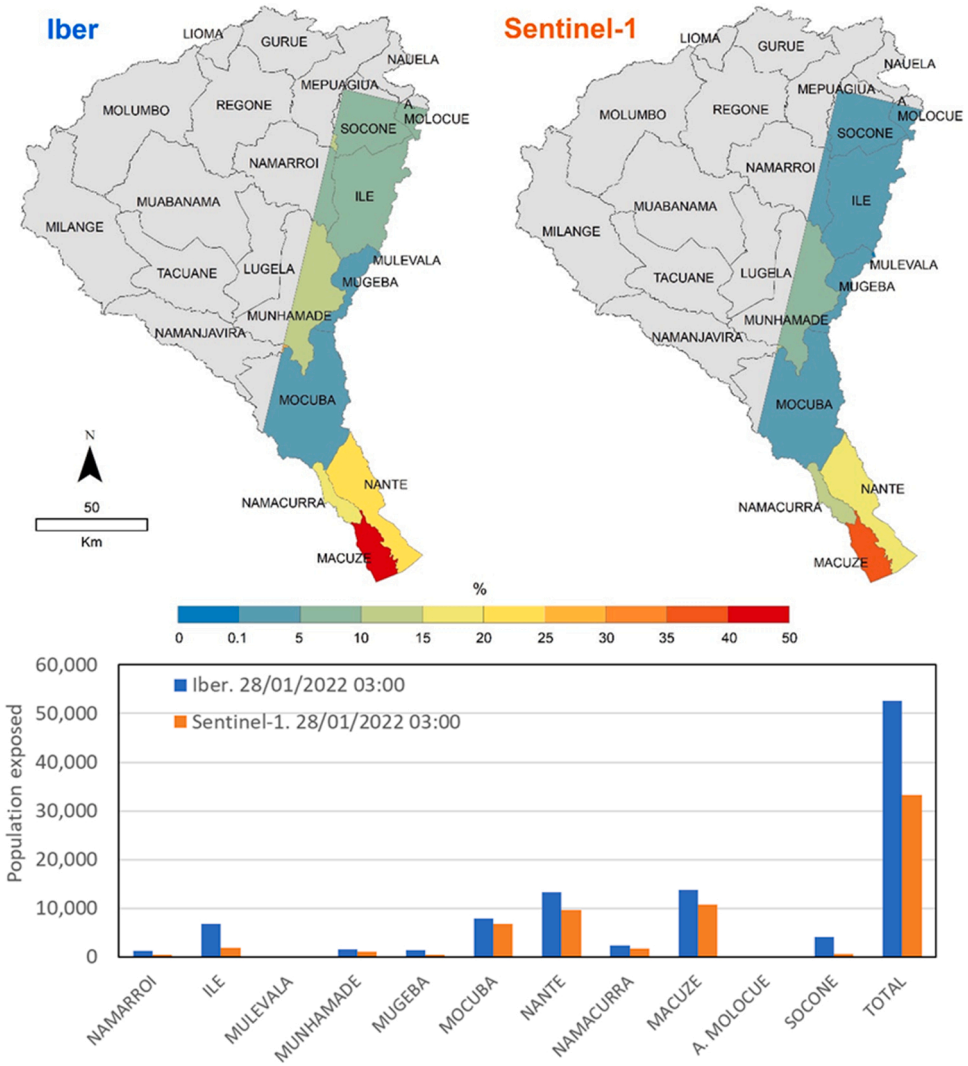

Fig. 12. Population exposed to flooding on 28/01/2022 at 03:00 at the different Administrative Posts of the Licungo basin, estimated from Sentinel-1 and from Iber (only in the area covered by Sentinel-1).

Table 5
Total population and population exposed to flooding at each Administrative Posts lying within the image of Sentinel-1. The exposed population is estimated on 28/01/2022 at 03:00 from Sentinel-1 image and from Iber (only in the area covered by Sentinel-1).

Administrative post	Total population	Exposed population (S1 coverage)	
		S1 28/01/2022	Iber 28/01/2022
NAMARROI	22,989	426	1260
ILE	139,115	1889	6818
MULEVALA	188	0	0
MUNHAMADE	14,981	1072	1562
MUGEBA	36,165	479	1359
MOCUBA	187,164	6713	7968
NANTE	57,617	9626	13,246
NAMACURRA	14,978	1660	2307
MACUZE	30,315	10,715	13,704
A. MOLOCUE	2242	12	155
SOCONE	61,813	610	4042
TOTAL	**567,568**	**33,203**	**52,419**

Fig. 13 shows the hydrographs computed with Iber at the basin outlet and at the confluence between the rivers Lugela and Licungo (Reach 1 in Fig. 11). According to the model, at the basin outlet the river discharge was approximately 2000 m^3/s at the time at which the Sentinel-1 image was taken, while the peak discharge occurred 51 h prior to this (26/01/2022 at 00:00) and was over 14,000 m^3/s, that is, seven times more. The difference is even greater at the confluence between the Licungo and Lugela, where the peak discharge reached 16,000 m^3/s, i.e., 16 times more than the 1000 m^3/s that were flowing when the Sentinel-1 image was taken. To illustrate the implications of these differences on the extension of the inundation, the middle and right panels of Fig. 9 show, respectively, the predictions of the flood extent obtained with Iber on 28/01/2022 at 03:00 and for the whole TS Ana event.

Even if these are simply numerical estimates, and the previous ratios might be slightly different in reality, they provide evidence that the number of people exposed to flooding during the whole event was much larger than the estimate obtained from the Sentinel-1 image. According to the numerical results for the whole catchment, over 273,000 people were exposed to flooding during the entire event. This is almost three times greater than the estimate made with Iber for the whole basin at the time when the Sentinel-1 image was taken (Table 6 and Fig. 14). In the lower part of the catchment, where the estimates obtained from Iber and Sentinel-1 are closer (Table 5), this ratio varies between 1.7 and 3.9 (see APs of Mocuba, Nante, Namacurra and Macuze in Table 6 and Fig. 14). In the upper catchment the ratio is even larger, reaching values higher than 4 in several APs. Although, as mentioned in Section 4.2, the numerical estimate of exposed population in the upper part of the catchment is less reliable than in the lower part, those ratios provide an approximation of the underestimation factor introduced when analysing the effects of the flood extent on 28/01/2022 at 03:00 rather than at the time of maximum flooding (Fig. 14 and Fig. 15).

If we now compare the estimates of people exposed to flooding in the whole catchment during the entire TS Ana event (273,937 people) with those corresponding to the date and area of the Sentinel-1 image (52,606 people), both obtained from Iber, it can be seen that there is a difference of a factor of 5.2, again implying that the estimate that can be drawn from the satellite image is just a small fraction of the real flood impact (Fig. 14).

It could be argued that the Iber-derived predictions of exposed population (273,937 people) might overpredict the actual number of people affected by the flood due to the inherent limitations of the numerical model's predictions. As an alternative to the estimate obtained directly from the numerical model, we can use the Iber-derived factors that relate the number of people exposed in the whole basin and/or during the whole TS Ana event with those exposed on 28/01/2022 at 03:00 within the area covered by the Sentinel-1 image, in order to extrapolate the satellite-derived estimate of exposed population to the whole event and catchment. The extrapolation of the satellite-derived estimates done in such a way are shown in Fig. 14 with an oblique fill pattern, in order to distinguish them from the direct estimates from the satellite image. Assuming that the numerical overestimation factor is similar during the whole event and for the whole catchment, the total exposed population would be about 5.2 times larger than the estimate obtained directly from Sentinel-1, leading to 172,655 (33,203 $\times$5.2) people that could have been exposed to the flood at some point during the TS Ana event.

It is difficult to assess which of the previous estimates (273,937 or 172,655 people) is more realistic, but the actual exposed population was probably somewhere between these two numbers, probably nearer to 273,000 than to 172,000, since the model's overprediction at the reach scale is not so high (Table 4). In any case, these figures are far more representative of the real number of people affected by the flood than the estimate that can be done using only the satellite imagery (33,244 people).

5. Conclusions

Estimation of the population affected by major flooding events in data-scarce regions, and especially by tropical storms in East Africa, is generally done on the basis of the analysis of satellite images. Such images are used to delineate the water extent and then

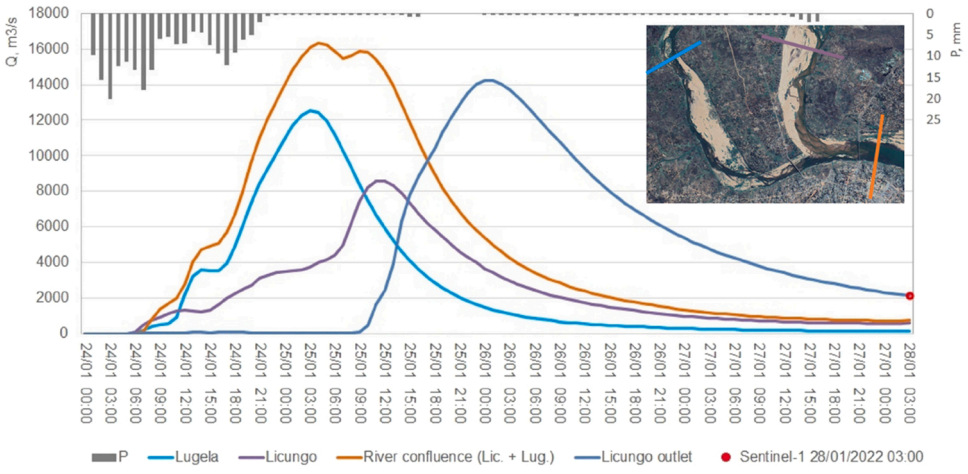

Fig. 13. Hydrographs computed with Iber during the TS Ana event, at the confluence between the Lugela and Licungo rivers (Reach 1 in Fig. 11), and at the outlet of the Licungo basin. Source of the satellite image on the top-right: Google earth V 7.3.4.8642. Imagery date: August 9, 2019. http://www.earth.google.com (Accessed September 26, 2022).

Table 6
Total population and population exposed to flooding at each Administrative Post for the whole Licungo basin. The exposed population is estimated on 28/01/2022 at 03:00 and for the whole TS Ana event. In both cases the estimates were obtained from Iber and for the whole Licungo basin. The last column indicates the ratio between the population exposed for the whole TS Ana and on 28/01/2022 at 03:00.

Administrative Post	Total population	Exposed population (whole Licungo basin)		
		Iber 28/01/2022 (A)	Iber Whole TS Ana (B)	Ratio (B/A)
MOLUMBO	36,483	1001	4544	4.54
REGONE	63,864	2262	8052	3.56
NAMARROI	114,280	6272	18,441	2.94
MILANGE	200,991	4208	26,925	6.40
MUABANAMA	77,658	3502	12,879	3.68
ILE	139,215	6723	19,113	2.84
LUGELA	54,038	2787	10,335	3.71
MULEVALA	190	0	7	–
TACUANE	26,921	1896	6511	3.43
MUNHAMADE	20,814	1961	6889	3.51
MUGEBA	35,963	1351	5844	4.32
NAMANJAVIRA	33,111	1336	6658	4.98
MOCUBA	200,082	8262	32,267	3.91
NANTE	57,586	13,210	22,751	1.72
NAMACURRA	14,933	2324	5255	2.26
MACUZE	30,423	13,742	24,332	1.77
LIOMA	5020	114	399	3.50
NAUELA	30,826	1673	5019	3.00
GURUE	194,384	12,578	30,816	2.45
MEPUAGIUA	87,525	5102	13,736	2.69
A. MOLOCUE	3310	219	576	2.63
SOCONE	72,403	4941	12,587	2.55
TOTAL	**1,500,019**	**95,467**	**273,937**	**2.87**

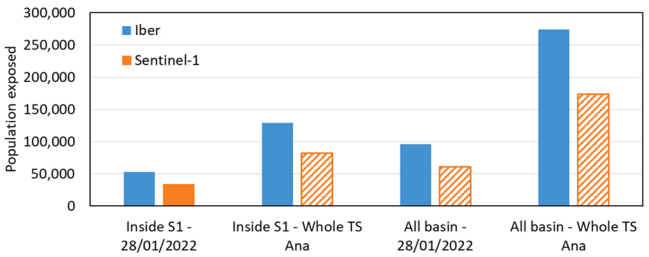

Fig. 14. Population exposed to flooding estimated from Iber and from Sentinel-1. Estimates inside the area covered by Sentinel-1, for the whole Licungo basin, on 28/01/2022 at 03:00 and for the whole TS Ana event are shown. The bars with an oblique fill pattern are indirect estimates obtained from the extrapolation of the Sentinel-1 image and the Iber estimates, as detailed in the text.

overlapped with population density maps in order to identify the areas most affected by a flood. While this procedure provides very useful and timely information for flood management, its main limitation is that the date and time at which the satellite image is available is usually not the time of maximum flooding, and therefore the water extent that can be derived from these images might be far smaller than the maximum flood extent. This is especially true during flash flood events in large catchments, as in the case study presented here, since the maximum flooding does not take place at the same time in the whole river network, but instead propagates progressively from the headwater subcatchments to the basin outlet. It is therefore not possible to capture the maximum flood extent in a single image. Moreover, large catchments might not be fully captured by the available satellite images during a single storm event, preventing an estimate of the flooded area in the whole basin.

Using an integrated hydrological-hydraulic modelling approach that relies in freely-available software and global satellite data, we have estimated the maximum flood extent during TS Ana in the whole Licungo catchment, and from that, the total population affected by the flood. We also estimated the area covered by the water during the flood recession, which was the time at which the satellite Sentinel-1 took an image of the east part of the basin. A comparison between the water extent computed with Iber and with Sentinel-1 showed a relatively good Hit Ratio (0.79) when considering the whole area of the basin covered by the satellite images. The False Alarm Ratio for the whole Sentinel-1 coverage was also high (0.60), but this value is overestimated, since most of the False Positives lie in tributaries of the Licungo and Lugela rivers that are not captured by the analysis of the satellite image. In the Licungo and Lugela rivers, where the water extension defined from Sentinel-1 is more reliable, the Hit Ratio is still of the order of 0.80, the FAR decreases to around 0.20 and there is no significant bias between the Iber and Sentinel-1 predictions.

The numerical results obtained with Iber indicate that over 273,000 people were exposed to flooding during the whole event in the whole catchment, while only around 95,000 people were being exposed at the time the Sentinel-1 image was taken, since the flood had

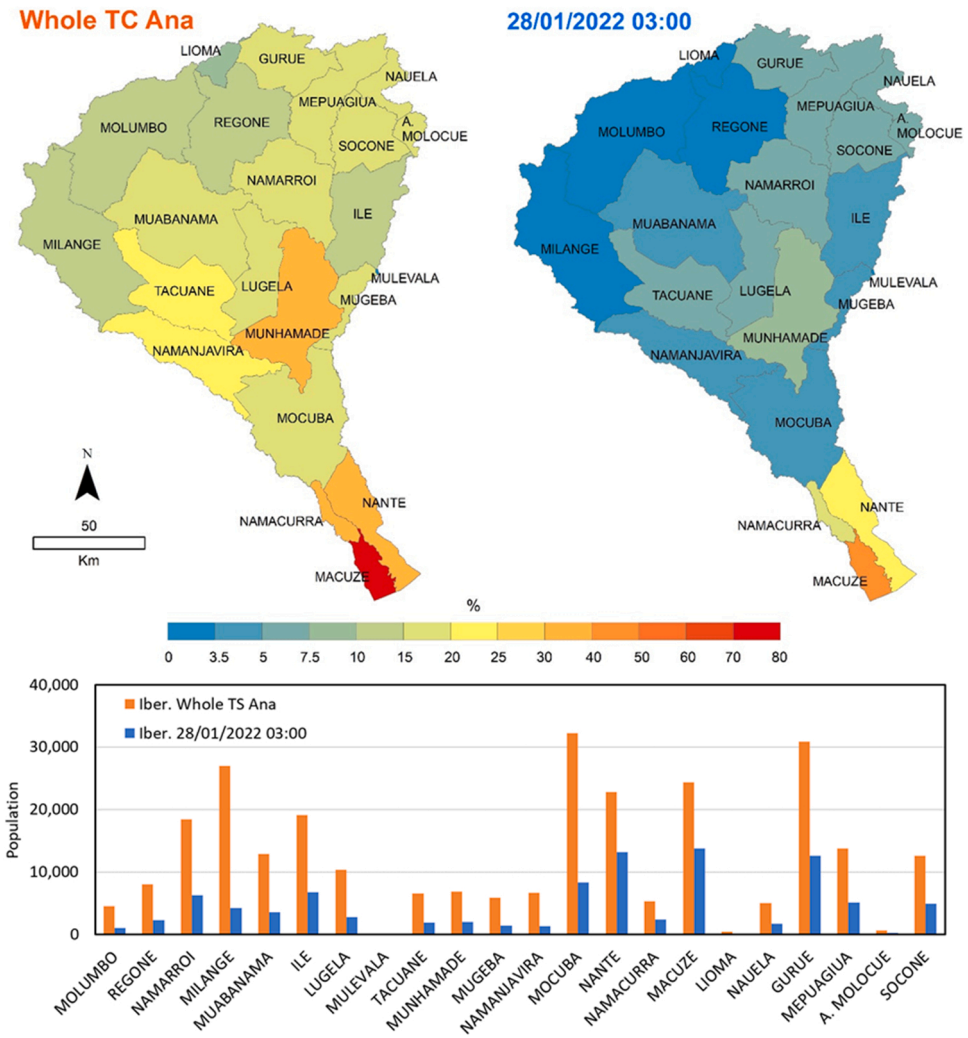

Fig. 15. Population exposed to flooding on 28/01/2022 at 03:00 and during the whole TS Ana event, at the different Administrative Posts of the Licungo basin, estimated from Iber. The final column shows the ratio between the exposed population during the whole TS Ana event and that recorded on 28/01/2022 at 03:00.

already been receding for more than 48 h by that time. Moreover, according to the numerical results, around 52,000 people were exposed to flooding inside the area covered by the Sentinel-1 image (around 28% of the total basin surface) at the time the image was taken. Even if those numbers are just numerical estimates, they contrast with the estimate of 33,000 people exposed to flooding obtained from the analysis of the satellite image alone, and are far more representative of the actual number of people affected by TS Ana in the Licungo basin.

The numerical methodology used in this study also provides estimates of the maximum water depths and velocities reached during the whole event in all the river network of the catchment. These estimates could be combined with vulnerability maps and damage curves in order to give a more detailed definition of flood risk and economical damages during a storm event. Such an analysis was not performed here due to the lack of detailed spatial information about vulnerability and stage-damage curves within the study region.

All the data sets used in this study are available for free and at the global scale, through the URLs provided in Section 3. The modelling software, Iber, is also available free of charge from www.iberaula.com. Thus, the methodology followed here can be reproduced in almost any region of the world, although it is especially suitable and interesting for the estimation of the effects of storm events in data-scarce regions.

CRediT authorship contribution statement

Luis Cea: Supervision, Conceptualization, Methodology, Software, Writing - original draft, Writing - review & editing. **Manuel Álvarez:** Conceptualization, Methodology, Validation, Visualization, Writing - original draft, Writing - review & editing. **Jerónimo Puertas:** Conceptualization, Methodology, Supervision.

Declaration of Competing Interest

The authors declare the following financial interests/personal relationships which may be considered as potential competing interests:Manuel Alvarez reports financial support was provided by Directorate-General for European Civil Protection and Humanitarian Operations (ECHO).

Data availability

Data will be made available on request.

Acknowledgements

The work presented in this paper began within the project "To strengthen national, district and local preparedness and response capacities, linking early warning to early action and fostering scalability of the action in Mozambique", with the participation of Spanish Red Cross, Mozambique Red Cross and the World Food Programme, and was supported financially by the Directorate-General for European Civil Protection and Humanitarian Operations (ECHO) within the Humanitarian Implementation Plan 2018 (ECHO/-SF/BUD/2018/91000). Funding for open access charge: Universidade da Coruña/CISUG.

Appendix A. Supporting information

Supplementary data associated with this article can be found in the online version at doi:10.1016/j.ejrh.2022.101247.

References

Abrams, M., 2000. The advanced spaceborne thermal emission and reflection radiometer (ASTER): data products for the high spatial resolution imager on NASA's Terra platform. Int. J. Remote Sens. 21 (5), 847–859.

Alfieri, L., Burek, P., Dutra, E., Krzeminski, B., Muraro, D., Thielen, J., Pappenberger, F., 2013. GloFAS-global ensemble streamflow forecasting and flood early warning. Hydrol. Earth Syst. Sci. 17 (3), 1161.

Álvarez, M., Puertas, J., Peña, E., Bermúdez, M., 2017. Two-dimensional dam-break flood analysis in data-scarce regions: the case study of Chipembe dam, Mozambique. Water 9 (6), 432.

Areu-Rangel, O.S., Cea, L., Bonasia, R., Espinosa-Echavarria, V.J., 2019. Impact of urban growth and changes in land use on river flood hazard in Villahermosa, Tabasco (Mexico). Water 11 (2), 304.

Arnell, N.W., Gosling, S.N., 2016. The impacts of climate change on river flood risk at the global scale. Clim. Change 134 (3), 387–401. https://doi.org/10.1007/s10584-014-1084-5.

Bayburt, S., Kurtak, A.B., Büyüksalih, G., Jacobsen, K., 2017. Geometric accuracy analysis of WorldDEM in relation to AW3D30, SRTM and ASTER GDEM2. International Archives of the Photogrammetry. Int. Arch. Photogramm. Remote Sens. Spat. Inf. Sci. -ISPRS Arch. 42 (2017), 211–217. Nr. 1W1, 42(1W1).

Bennett, N.D., Croke, B.F., Guariso, G., Guillaume, J.H., Hamilton, S.H., Jakeman, A.J., Andreassian, V., 2013. Characterising performance of environmental models. Environ. Model. Softw. 40, 1–20. https://doi.org/10.1016/j.envsoft.2012.09.011.

Bermúdez, M., Neal, J.C., Bates, P.D., Coxon, G., Freer, J.E., Cea, L., Puertas, J., 2017. Quantifying local rainfall dynamics and uncertain boundary conditions into a nested regional-local flood modelling system. Water Resour. Res. 53, 2770–2785.

Bermúdez, M., Cea, L., Puertas, J., 2019. A rapid flood inundation model for hazard mapping based on least squares support vector machine regression. J. Flood Risk Manag. 12, e12522.

Bladé, E., Cea, L., Corestein, G., Escolano, E., Puertas, J., Vázquez-Cendón, M.E., Dolz, J., Coll, A., 2014. Iber: herramienta de simulación numérica del flujo en ríos. Rev. Int. De. Métodos Numér Para. Cálculo Y. Diseño En. Ing. 30 (1), 1–10.

Caletka, M., Šulc Michalková, M., Karásek, P., Fučík, P., 2020. Improvement of SCS-CN initial abstraction coefficient in the Czech Republic: a study of five catchments. Water 12 (7), 1964.

Calka, B., Nowak Da Costa, J., Bielecka, E., 2017. Fine scale population density data and its application in risk assessment. Geomat. Nat. Hazard. Risk 8 (2), 1440–1455.

Cao, W., Zhou, Y., Güneralp, B., Li, X., Zhao, K., Zhang, H., 2022. Increasing global urban exposure to flooding: an analysis of long-term annual dynamics. Sci. Total Environ. 817, 153012.

Cea, L., Blade, E., 2015. A simple and efficient unstructured finite volume scheme for solving the shallow water equations in overland flow applications. Water Resour. Res. 51 (7), 5464–5486.

Cea, L., Costabile, P., 2022. Flood risk in urban areas: modelling, management and adaptation to climate change. A Rev. Hydrol. 9 (3), 50.

Cea, L., Fraga, I., 2018. Incorporating antecedent moisture conditions and intraevent variability of rainfall on flood frequency analysis in poorly gauged basins. Water Resour. Res. 54 (11), 8774–8791.

Cea, L., Legout, C., Grangeon, T., Nord, G., 2016. Impact of model simplifications on soil erosion predictions: application of the GLUE methodology to a distributed event-based model at the hillslope scale. Hydrol. Process. 30 (7), 1096–1113.

Cools, J., Vanderkimpen, P., El Afandi, G., Abdelkhalek, A., Fockedey, S., El Sammany, M., Huygens, M., 2012. An early warning system for flash floods in hyper-arid Egypt. Nat. Hazards Earth Syst. Sci. 12 (2), 443–457.

Cornelissen, T., Diekkrüger, B., Giertz, S., 2013. A comparison of hydrological models for assessing the impact of land use and climate change on discharge in a tropical catchment. J. Hydrol. 498, 221–236.

Costabile, P., Costanzo, C., Ferraro, D., Macchione, F., Petaccia, G., 2020. Performances of the new HEC-RAS version 5 for 2-D hydrodynamic-based rainfall-runoff simulations at basin scale: comparison with a state-of-the art model. Water 12 (9), 2326.

CRED (2022). The International Disaster Database [online], Centre for Research on the Epidemiology of Disasters. Available online from: https://public.emdat.be (accessed on 13 March 2022).

Curtis, S., Crawford, T.W., Lecce, S.A., 2007. A comparison of TRMM to other basin-scale estimates of rainfall during the 1999 Hurricane Floyd flood. Nat. Hazards 43 (2), 187–198.

Dahmm, H., Rabiee M., Espey, J., Adamo, S., 2020. Leaving no one off the map: a guide for gridded population data for sustainable development. https://www.unsdsn.org/leaving-no-one-off-the-map-a-guide-for-gridded-population-data-for-sustainable-development.

Di Baldassarre, G., Schumann, G., Bates, P.D., 2009. A technique for the calibration of hydraulic models using uncertain satellite observations of flood extent. J. Hydrol. 367 (3–4), 276–282.
Di Baldassarre, G., Montanari, A., Lins, H., Koutsoyiannis, D., Brandimarte, L., Blöschl, G., 2010. Flood fatalities in Africa: from diagnosis to mitigation. Geophys. Res. Lett. 37 https://doi.org/10.1029/2010GL045467.
Di Mauro, C., Hostache, R., Matgen, P., Pelich, R., Chini, M., Van Leeuwen, P.J., Blöschl, G., 2021. Assimilation of probabilistic flood maps from SAR data into a coupled hydrologic–hydraulic forecasting model: a proof of concept. Hydrol. Earth Syst. Sci. 25 (7), 4081–4097.
Domeneghetti, A., Tarpanelli, A., Brocca, L., Barbetta, S., Moramarco, T., Castellarin, A., Brath, A., 2014. The use of remote sensing-derived water surface data for hydraulic model calibration. Remote Sens. Environ. 149, 130–141.
Dottori, F., Salamon, P., Bianchi, A., Alfieri, L., Hirpa, F.A., Feyen, L., 2016. Development and evaluation of a framework for global flood hazard mapping. Adv. Water Resour. 94, 87–102.
Douglas, I., Kurshid, A., Maghenda, M., McDonnell, Y., McLean, L., Campbell, J., 2008. Unjust waters: climate change, flooding and the urban poor in Africa. Environ. Urban. 20 (1), 187–205. https://doi.org/10.1177/0956247808089156.
DRRT, 2015. Dutch Risk Reduction Team: Reducing the risk of water related disasters. Flood Control in the Licungo Basin of Zambezi Province. DRR-Team Scoping Mission, Final Report, 15 June 2015. Kingdom of the Netherlands.
Eilander, D., Couasnon, A., Leijnse, T., Ikeuchi, H., Yamazaki, D., Muis, S., Ward, P.J., 2022. A globally-applicable framework for compound flood hazard modeling. EGUsphere 1–40.
ESA. (2017). Land Cover CCI Product User Guide Version 2. Tech. Rep. (2017). Available at: maps.elie.ucl.ac.be/CCI/viewer/download/ESACCI-LC-Ph2-PUGv2_2.0.pdf.
Falter, D., Vorogushyn, S., Lhomme, J., Apel, H., Gouldby, B., Merz, B., 2013. Hydraulic model evaluation for large-scale flood risk assessments. Hydrol. Process. 27 (9), 1331–1340.
Farr, T.G., Rosen, P.A., Caro, E., Crippen, R., Duren, R., Hensley, S., et al., 2007. The shuttle radar topography mission. Rev. Geophys. 45, RG2004. https://doi.org/10.1029/2005RG000183.1.
Fernández-Nóvoa, D., García-Feal, O., González-Cao, J., de Gonzalo, C., Rodríguez-Suárez, J.A., Ruiz del Portal, C., Gómez-Gesteira, M., 2020. MIDAS: a new integrated flood early warning system for the Miño river. Water 12 (9), 2319.
Fraga, I., Cea, L., Puertas, J., 2019. Effect of rainfall uncertainty on the performance of physically-based rainfall-runoff models. Hydrol. Process. 33 (1), 160–173.
Fraga, I., Cea, L., Puertas, J., 2020. MERLIN: a flood hazard forecasting system for coastal river reaches. Nat. Hazards 100, 1171–1193. https://doi.org/10.1007/s11069-020-03855-7.
Funk, C., Peterson, P., Landsfeld, M., Pedreros, D., Verdin, J., Shukla, S., Michaelsen, J., 2015. The climate hazards infrared precipitation with stations – a new environmental record for monitoring extremes. Sci. Data 2 (1), 1–21.
García-Feal, O., González-Cao, J., Gómez-Gesteira, M., Cea, L., Domínguez, J.M., Formella, A., 2018. An accelerated tool for flood modelling based on Iber. Water 10 (10), 1459. https://doi.org/10.3390/w10101459.
Garrote, J., 2022. Free global DEMs and flood modelling-a comparison analysis for the January 2015 flooding event in Mocuba city (Mozambique). Water 14 (2), 176.
GDACS2022a. Overall orange alert tropical cyclone for ANA-22 in Mozambique, Malawi, Miscellaneous (French) Indian Ocean Islands, Madagascar, Zimbabwe. GDACS: Global Disaster Alert and Coordination System, United Nations and the European Commission. https://www.gdacs.org/report.aspx?eventid=1000858&episodeid=3&eventtype=TC.
GDACS, 2022b. Overall orange alert tropical cyclone for GOMBE-22 in Madagascar and Mozambique. GDACS: Global disaster alert and coordination system, United Nations and the European Commission. https://www.gdacs.org/report.aspx?eventid=1000873&episodeid=14&eventtype=TC.
González-Cao, J., García-Feal, O., Fernández-Nóvoa, D., Domínguez-Alonso, J.M., Gómez-Gesteira, M., 2019. Towards an automatic early warning system of flood hazards based on precipitation forecast: the case of the Miño River (NW Spain). Nat. Hazards Earth Syst. Sci. 19, 11.
Grimaldi, S., Li, Y., Pauwels, V., Walker, J.P., 2016. Remote sensing-derived water extent and level to constrain hydraulic flood forecasting models: opportunities and challenges. Surv. Geophys. 37 (5), 977–1034.
Guth, P.L., Geoffroy, T.M., 2021. LiDAR point cloud and ICESat-2 evaluation of 1 second global digital elevation models: copernicus wins. Trans. GIS 25 (5), 2245–2261.
Harris, A., Rahman, S., Hossain, F., Yarborough, L., Bagtzoglou, A.C., Easson, G., 2007. Satellite-based flood modeling using TRMM-based rainfall products. Sensors 7 (12), 3416–3427.
Hirabayashi, Y., Mahendran, R., Koirala, S., Konoshima, L., Yamazaki, D., Watanabe, S., Kim, H., Kanae, S., 2013. Global flood risk under climate change. Nat. Clim. Change 3 (9), 816–821. https://doi.org/10.1038/nclimate1911.
Hong, Y., Hsu, K.L., Sorooshian, S., Gao, X.G., 2004. Precipitation estimation from remotely sensed imagery using an artificial neural network cloud classification system. J. Appl. Meteorol. 43 (12), 1834–1852. ⟨https://escholarship.org/uc/item/2x4152rx⟩.
Hope, A.S., Schulze, R.E., 1982. Improved estimates of stormflow volume using the SCS curve number method. In: Singh, V.P. (Ed.), Rainfall Runoff Relationships. Water Resources Publications, Littleton, pp. 419–431.
Hsu, K.-L., Sorooshian, S., 2008. Satellite-based precioppitation measurement using PERSIANN system. In: Sorooshian, S., Hsu, K.-L., Coppola, E., Tomassetti, B., Verdecchia, M., Visconti, G. (Eds.), Hydrological Modelling and the Water Cycle: Coupling the Atmospheric and Hydrological Models. Springer, Berlin Heidelberg. https://doi.org/10.1007/978-3-540-77843-1_2.
Huang, M., Gallichand, J., Dong, C., Wang, Z., Shao, M., 2007. Use of soil moisture data and curve number method for estimating runoff in the Loess Plateau of China. Hydrol. Process.: Int. J. 21 (11), 1471–1481.
Huffman, G.J., Bolvin, D.T., Nelkin, E.J., Wolff, D.B., Adler, R.F., Gu, G., Hong, Y., Bowman, K.P., Stocker, E.F., 2007. The TRMM multisatellite precipitation analysis (TMPA): quasi-global, multiyear, combined-sensor precipitation estimates at fine scales. J. Hydrometeorol. 8 (1), 38–55.
Huffman, G.J., Bolvin, D.T., Braithwaite, D., Hsu, K.-L., Joyce, R.J., Kidd, C., Nelkin, E.J., Sorooshian, S., Stocker, E.F., Tan, J., 2020. Integrated multi-satellite retrievals for the global precipitation measurement (GPM) mission (IMERG). Satellite Precipitation Measurement. Springer International Publishing, pp. 343–353. https://doi.org/10.1007/978–3-030–24568-9_19.
Institute for Economics and Peace , 2021. Ecological Threat Report 2021: Understanding Ecological Threats, Resilience and Peace, Sydney, October 2021. Available from: http://visionofhumanity.org/resources (accessed 15 March 2022).
Jaafar, Hadi H., Farah, A.Ahmad, Beyrouthy, Naji El, 2019. GCN250, new global gridded curve numbers for hydrologic modeling and design. Sci. Data 6 (1), 145.
Jenkins, K., Surminski, S., Hall, J., Crick, F., 2017. Assessing surface water flood risk and management strategies under future climate change: insights from an agent-based model. Sci. Total Environ. 595, 159–168.
Jongman, B., Ward, P.J., Aerts, J.C.J.H., 2012. Global exposure to river and coastal flooding: long term trends and changes. Glob. Environ. Change 22, 823–835. https://doi.org/10.1016/j.gloenvcha.2012.07.004.
Khaing, Z.M., Zhang, K., Sawano, H., Shrestha, B.B., Sayama, T., Nakamura, K., 2019. Flood hazard mapping and assessment in data-scarce Nyaungdon area. Myanmar PLOS One 14 (11), e0224558.
Komi, K., Neal, J., Trigg, M.A., Diekkrüger, B., 2017. Modelling of flood hazard extent in data sparse areas: a case study of the Oti River basin. West Afr. J. Hydrol.: Reg. Stud. 10, 122–132.
Krajewski, W.F., Ceynar, D., Demir, I., Goska, R., Kruger, A., Langel, C., Young, N.C., 2017. Real-time flood forecasting and information system for the state of Iowa. Bull. Am. Meteorol. Soc. 98 (3), 539–554.
Krieger, G., Zink, M., Bachmann, M., Bräutigam, B., Schulze, D., Martone, M., Moreira, A., 2013. TanDEM-X: a radar interferometer with two formation-flying satellites. Acta Astronaut. 89, 83–98.
Kubota, T., Shige, S., Hashizume, H., Aonashi, K., Takahashi, N., Seto, S., Hirose, M., Takayabu, Y.N., Ushio, T., Nakagawa, K., Iwanami, K., Kachi, M., Okamoto, K., 2007. Global precipitation map using satellite-borne microwave radiometers by the GSMaP project: production and validation. IEEE Trans. Geosci. Remote Sens. 45 (7), 2259–2275. https://doi.org/10.1109/TGRS.2007.895337.

Kundu, S., Aggarwal, S.P., Kingma, N., Mondal, A., Khare, D., 2015. Flood monitoring using microwave remote sensing in a part of Nuna river basin. Odisha, India. Natural hazards 76 (1), 123–138.
Kugler, Z., De Groeve, T., 2007. The global flood detection system. Office for Official Publications of the European Communities, Luxembourg.
Kuntla, S.K., Manjusree, P., 2020. Development of an automated tool for delineation of flood footprints from sar imagery for rapid disaster response: a case study. J. Indian Soc. Remote Sens. 48 (6), 935–944.
Lehner, B., Verdin, K., Jarvis, A., 2008. New global hydrography derived from spaceborne elevation data. In: Eos, Transactions, 89. American Geophysical Union,, pp. 93–94. https://doi.org/10.1029/2008eo100001.
Leopold, L.B., Maddock, T., 1953. The Hydraulic Geometry of Stream Channels and Some Physiographic Implications, Vol. 252. US Government Printing Office,.
Leyk, S., Gaughan, A.E., Adamo, S.B., de Sherbinin, A., Balk, D., Freire, S., Rose, A., Stevens, F.R., Blankespoor, B., Frye, C., Comenetz, J., Sorichetta, A., MacManus, K., Pistolesi, L., Levy, M., Tatem, A.J., Pesaresi, M., 2019. The spatial allocation of population: a review of large-scale gridded population data products and their fitness for use. Earth Syst. Sci. Data 11 (3), 1385–1409. https://doi.org/10.5194/essd-11-1385-2019.
Li, L., Hong, Y., Wang, J., Adler, R.F., Policelli, F.S., Habib, S., Okello, L., 2009. Evaluation of the real-time TRMM-based multi-satellite precipitation analysis for an operational flood prediction system in Nzoia Basin. Lake Vic., Afr. Nat. Hazards 50 (1), 109–123.
Liu, H., Wang, Y., Zhang, C., Chen, A.S., Fu, G., 2018. Assessing real options in urban surface water flood risk management under climate change. Nat. Hazards 94 (1), 1–18.
Liu, J., Du, J., Yang, Y., Wang, Y., 2020. Evaluating extreme precipitation estimations based on the GPM IMERG products over the Yangtze River Basin, China. Geomat. Nat. Hazards Risk 11 (1), 601–618. https://doi.org/10.1080/19475705.2020.1734103.
Mareśová, J., Gdulová, K., Pracná, P., Moravec, D., Gábor, L., Prošek, J., Moudrý, V., 2021. Applicability of data acquisition characteristics to the identification of local artefacts in global digital elevation models: comparison of the Copernicus and TanDEM-X DEMs. Remote Sens. 13 (19), 3931.
Merz, R., Parajka, J., Blöschl, G., 2011. Time stability of catchment model parameters: implications for climate impact analyses. Water Resour. Res. 47, W02531. https://doi.org/10.1029/2010WR009505.
Mishra, S.K., Singh, V., 2003. Soil Conservation Service Curve Number (SCS-CN) Methodology, vol.42. Springer Science & Business Media.
Neal, J., Schumann, G., Bates, P., 2012. A subgrid channel model for simulating river hydraulics and floodplain inundation over large and data sparse areas. Water Resour. Res. 48, 11.
Nogherotto, R., Fantini, A., Raffaele, F., Di Sante, F., Dottori, F., Coppola, E., Giorgi, F., 2019. An integrated hydrological and hydraulic modelling approach for the flood risk assessment over Po river basin. Natural Hazards and Earth System Sciences Discussions 1–22.
Nemni, E., Bullock, J., Belabbes, S., Bromley, L., 2020. Fully convolutional neural network for rapid flood segmentation in synthetic aperture radar imagery. Remote Sens. 12 (16) https://doi.org/10.3390/rs12162532.
Nguyen, P., Ombadi, M., Sorooshian, S., Hsu, K., AghaKouchak, A., Braithwaite, D., Ashouri, H., Thorstensen, A.R., 2018. The PERSIANN family of global satellite precipitation data: a review and evaluation of products. Hydrol. Earth Syst. Sci. 22 (11), 5801–5816. https://doi.org/10.5194/hess-22-5801-2018.
OCHA. 2022c. Mozambique: tropical cyclone gombe flash update No.8 (As of 1 April 2022). Situation Report. https://reliefweb.int/report/mozambique/mozambique-tropical-cyclone-gombe-flash-update-no8–1-april-2022.
OCHA. 2022a. Mozambique: tropical storm ana flash update No.9 (As of 14 February 2022). Situation Report. https://reliefweb.int/report/mozambique/mozambique-tropical-storm-ana-flash-update-no9–14-february-2022.
OCHA2022b. Mozambique: tropical storms ana and dumako flash update No.10 (As of 2 March 2022). Situation Report. https://reliefweb.int/report/mozambique/mozambique-tropical-storms-ana-and-dumako-flash-update-no10–2-march-2022.
O'Loughlin, F.E., Paiva, R.C., Durand, M., Alsdorf, D.E., Bates, P.D., 2016. A multi-sensor approach towards a global vegetation corrected SRTM DEM product. Remote Sens. Environ. 182, 49–59.
Pappenberger, F., Cloke, H.L., Balsamo, G., Ngo-Duc, T., Oki, T., 2010. Global runoff routing with the hydrological component of the ECMWF NWP system. Int. J. Climatol. 30 (14), 2155–2174. https://doi.org/10.1002/joc.2028.
Pradhan, R.K., Markonis, Y., Vargas Godoy, M.R., Villalba-Pradas, A., Andreadis, K.M., Nikolopoulos, E.I., Papalexiou, S.M., Rahim, A., Tapiador, F.J., Hanel, M., 2022. Review of GPM IMERG performance: a global perspective. Remote Sens. Environ. 268, 112754 https://doi.org/10.1016/J.RSE.2021.112754.
Rentschler, J., Avner, P., Marconcini, M., Su, R., Strano, E., Hallegatte, S., Bernard, L., & Riom, C.2022. Rapid Urban Growth in Flood Zones: Global Evidence since 1985. Policy Research Working Paper; 10014. World Bank, Washington, DC. https://openknowledge.worldbank.org/handle/10986/37348 License: CC BY 3.0 IGO.
Revilla-Romero, B., Thielen, J., Salamon, P., De Groeve, T., Brakenridge, G.R., 2014. Evaluation of the satellite-based global flood detection system for measuring river discharge: influence of local factors. Hydrol. Earth Syst. Sci. Discuss. 11, 7.
Rizzoli, P., Martone, M., Gonzalez, C., Wecklich, C., Tridon, D.B., Bräutigam, B., Moreira, A., 2017. Generation and performance assessment of the global TanDEM-X digital elevation model. ISPRS J. Photogramm. Remote Sens. 132, 119–139.
Ross, C.W., Prihodko, L., Anchang, J., Kumar, S., Ji, W., Hanan, N.P., 2018. HYSOGs250m, global gridded hydrologic soil groups for curve-number-based runoff modeling. Sci. Data 5 (1), 1–9.
Sakamoto, T., Van Nguyen, N., Kotera, A., Ohno, H., Ishitsuka, N., Yokozawa, M., 2007. Detecting temporal changes in the extent of annual flooding within the Cambodia and the Vietnamese Mekong Delta from MODIS time-series imagery. Remote Sens. Environ. 109, 295–313.
Sanyal, J., Carbonneau, P., Densmore, A.L., 2014. Low-cost inundation modelling at the reach scale with sparse data in the Lower Damodar River basin. India. Hydrological Sciences Journal 59 (12), 2086–2102.
Sampson, C.C., Smith, A.M., Bates, P.D., Neal, J.C., Alfieri, L., Freer, J.E., 2015. A high-resolution global flood hazard model. Water resources research, 51 (9), 7358–7381.
Sanz-Ramos, M., Amengual, A., Bladé, E., Romero, R., and Roux, H., 2018. Flood forecasting using a coupled hydrological and hydraulic model (based on FVM) and high resolution Meteorological Model. River Flow 2018 - Ninth International Conference on Fluvial Hydraulics. E3S Web of Conferences 40 (September): 06028.
Sanz-Ramos, M., Bladé, E., González-Escalona, F., Olivares, G., Aragón-Hernández, J.L., 2021. Interpreting the manning roughness coefficient in overland flow simulations with coupled hydrological-hydraulic distributed models. Water 13 (23), 3433.
Schumann, G.J.P., Moller, D.K., 2015. Microwave remote sensing of flood inundation. Phys. Chem. Earth, Parts A/B/C. 83, 84–95. https://doi.org/10.1016/j.pce.2015.05.002.
Shi, W., Wang, N., 2020. An improved SCS-CN method incorporating slope, soil moisture, and storm duration factors for runoff prediction. Water 12 (5), 1335.
Smith, A., Bates, P.D., Wing, O., Sampson, C., Quinn, N., Neal, J., 2019. New estimates of flood exposure in developing countries using high-resolution population data. Nat. Commun. 10 (1), 1–7.
Soulis, K.X., 2021. Soil conservation service curve number (SCS-CN) Method: current applications, remaining challenges, and future perspectives. Water 13 (2), 192.
Stevens, F., Gauhan, A., Linard, C., Tatem, A., 2015. Disaggregating census data for population mapping using random forests with remotely-sensed and ancillary data. PLOS One 10 (2), 1–22. https://doi.org/10.1371/journal.pone.0107042.
Sun, W., Ishidaira, H., Bastola, S., 2012. Calibration of hydrological models in ungauged basins based on satellite radar altimetry observations of river water level. Hydrol. Process. 26, 3524–3537.
Tramblay, Y., Amoussou, E., Dorigo, W., Mahé, G., 2014. Flood risk under future climate in data sparse regions: Linking extreme value models and flood generating processes. Journal of hydrology 519, 549–558.
Tadono, T., Ishida, H., Oda, F., Naito, S., Minakawa, K., Iwamoto, H., 2014. Precise global DEM generation by ALOS PRISM. ISPRS Ann. Photogramm. Remote Sens. Spatial. Inf. Sci. 2 (4), 71.
Tamagnone, P., Cea, L., Comino, E., Rosso, M., 2020. Rainwater harvesting techniques to face water scarcity in African's drylands: hydrological efficiency assessment. Water 12 (9), 2646.
Tate, E., Rahman, M.A., Emrich, C.T., Sampson, C.C., 2021. Flood exposure and social vulnerability in the United States. Nat. Hazards 106 (1), 435–457.
Tatem, A.J., 2017. WorldPop, open data for spatial demography. Sci. Data 4 (1), 170004. https://doi.org/10.1038/sdata.2017.4.

Tekeli, A.E., Fouli, H., 2016. Evaluation of TRMM satellite-based precipitation indexes for flood forecasting over Riyadh City. Saudi Arab. J. Hydrol. 541, 471–479.
Teng, J., Jakeman, A.J., Vaze, J., Croke, B.F., Dutta, D., Kim, S.J.E.M., 2017. Flood inundation modelling: a review of methods, recent advances and uncertainty analysis. Environ. Model. Softw. 90, 201–216.
Thielen, J., Bartholmes, J., Ramos, M.H., Roo, A.D., 2009. The European flood alert system–part 1: concept and development. Hydrol. Earth Syst. Sci. 13 (2), 125–140.
Uber, M., Nord, G., Legout, C., Cea, L., 2021. How do modeling choices and erosion zone locations impact the representation of connectivity and the dynamics of suspended sediments in a multi-source soil erosion model? Earth Surface. Dynamics 9, 123–144.
Watik, N., Jaelani, L.M., 2019. Flood evacuation routes mapping based on-flood impact analysis from landsat 8 imagery using network analyst method. ISPRS-Int. Arch. Photogramm. Remote Sens. Spatial. Inf. Sci. 4238, 455–460.
Weerts, A.H., Winsemius, H.C., Verkade, J.S., 2011. Estimation of predictive hydrological uncertainty using quantile regression: examples from the national flood forecasting system (England and Wales). Hydrol. Earth Syst. Sci. 15 (1), 255–265.
Wing, O.E., Bates, P.D., Sampson, C.C., Smith, A.M., Johnson, K.A., Erickson, T.A., 2017. Validation of a 30 m resolution flood hazard model of the conterminous United States. Water Resour. Res. 53 (9), 7968–7986.
Wing, O.E., Bates, P.D., Smith, A.M., Sampson, C.C., Johnson, K.A., Fargione, J., Morefield, P., 2018. Estimates of present and future flood risk in the conterminous United States. Environ. Res. Lett. 13 (3), 034023.
Winsemius, H.C., Van Beek, L.P.H., Jongman, B., Ward, P.J., Bouwman, A., 2013. A framework for global river flood risk assessments. Hydrol. Earth Syst. Sci. 17, 1871–1892. https://doi.org/10.5194/hess-17-1871-2013.
WMO2019. Reducing vulnerability to extreme hydro-meteorological hazards in Mozambique after Cyclone IDAI. WMO mission report following tropical cyclone IDAI (29 April to 7 May). World Meteorological Organization, Geneva.
World Bank2019a. Mozambique disaster risk management and resilience program: technical assessment report. World Bank, Washington, DC.
World Bank2019b. Mozambique Disaster Risk Profile. World Bank, Washington, DC.
WorldPop2018. (www.worldpop.org - School of Geography and Environmental Science, University of Southampton; Department of Geography and Geosciences, University of Louisville; Departement de Geographie, Universite de Namur) and Center for International Earth Science Information Network (CIESIN), Columbia University (2018). Global High Resolution Population Denominators Project - Funded by The Bill and Melinda Gates Foundation (OPP1134076). https://dx.doi.org/10.5258/SOTON/WP00645.
Wu, H., Adler, R.F., Tian, Y., Huffman, G.J., Li, H., Wang, J., 2014. Real-time global flood estimation using satellite-based precipitation and a coupled land surface and routing model. Water Resour. Res. 50, 2693–2717.
Xia, X., Liang, Q., Ming, X., 2019. A full-scale fluvial flood modelling framework based on a high-performance integrated hydrodynamic modelling system (HiPIMS). Adv. Water Resour. 132, 103392.
Yamazaki, D., Kanae, S., Kim, H., Oki, T., 2011. A physically based description of floodplain inundation dynamics in a global river routing model. Water Resour. Res. 47, W04501. https://doi.org/10.1029/2010WR009726.
Yamazaki, D., Ikeshima, D., Tawatari, R., Yamaguchi, T., O'Loughlin, F., Neal, J.C., Bates, P.D., 2017. A high-accuracy map of global terrain elevations. Geophys. Res. Lett. 44 (11), 5844–5853.
Yang, Y., Du, J., Cheng, L., Xu, W., 2017. Applicability of TRMM satellite precipitation in driving hydrological model for identifying flood events: a case study in the Xiangjiang River Basin, China. Nat. Hazards 87 (3), 1489–1505.
Zhao, J., Pelich, R., Hostache, R., Matgen, P., Cao, S., Wagner, W., Chini, M., 2021. Deriving exclusion maps from C-band SAR time-series in support of floodwater mapping. Remote Sens. Environ. 265, 112668.
Zink, M., Moreira, A., Hajnsek, I., Rizzoli, P., Bachmann, M., Kahle, R., Wessel, B., 2021. TanDEM-X: 10 years of formation flying bistatic SAR interferometry. IEEE J. Sel. Top. Appl. Earth Obs. Remote Sens. 14, 3546–3565.
Zuhlke, M., Fomferra, N., Brockmann, C., Peters, M., Veci, L., Malik, J., & Regner, P.2015. SNAP (sentinel application platform) and the ESA sentinel 3 toolbox. In: Proceedings of the Sentinel-3 for Science Workshop (Vol. 734, p. 21).